# The local environment of the activator ions in the solid-state lighting phosphor $Y_{3-x}Ce_xAl_5O_{12}$[†]

Nathan George,[‡,@] Géraldine Dantelle,[¶] A. J. Pell,[§] Katharine Page,[‖] Anna Llobet,[‖] M. Balasubramanian,[⊥] Bradley F. Chmelka,[*,‡] and Ram Seshadri[*,#,@]

*Department of Chemical Engineering, University of California, Santa Barbara, CA, 93106, USA, Laboratoire de Physique de la Matière Condensée, École Polytechnique, UMR 7643 CNRS, F-91128 Palaiseau, France, Centre de RMN à Trés Hauts Champs, UMR 5280 CNRS/Ecole Normale Supérieure de Lyon, University of Lyon, Villeurbanne, France, Los Alamos National Laboratory, Lujan Neutron Science Center, MS H805, Los Alamos, NM 87545, USA, X-ray Science Division, Advanced Photon Source, Argonne National Laboratory, Argonne, IL 60439, USA, and Materials Department and Materials Research Laboratory, University of California, Santa Barbara, CA, 93106, USA*

E-mail: bradc@engineering.ucsb.edu; seshadri@mrl.ucsb.edu

Phone: (805) 893-6129. Fax: (805) 893-8797

---

[†] Electronic supplementary information (ESI) available: Further details. See DOI: xx.xxxx/xxxxxxxxxx

[*] To whom correspondence should be addressed

[‡] Department of Chemical Engineering, University of California, Santa Barbara, CA, 93106, USA

[¶] Laboratoire de Physique de la Matière Condensée, École Polytechnique, UMR 7643 CNRS, F-91128 Palaiseau, France

[§] Centre de RMN à Trés Hauts Champs, UMR 5280 CNRS/Ecole Normale Supérieure de Lyon, University of Lyon, Villeurbanne, France

[‖] Los Alamos National Laboratory, Lujan Neutron Science Center, MS H805, Los Alamos, NM 87545, USA

[⊥] X-ray Science Division, Advanced Photon Source, Argonne National Laboratory, Argonne, IL 60439, USA

[#] Materials Department and Materials Research Laboratory, University of California, Santa Barbara, CA, 93106, USA

[@] Mitsubishi Chemical Center for Advanced Materials, University of California, Santa Barbara, CA, 93106, USA

# Abstract

In the luminescent cerium-doped yttrium aluminum garnet $Y_{3-x}Ce_xAl_5O_{12}$ (YAG:Ce) material, the crucial energy conversion that makes it such an important material in solid state white lighting is associated with the few percent of Y sites that are substituted by $Ce^{3+}$ activator ions. Despite the low levels of $Ce^{3+}$ substitution, the precise geometry of ions around $Ce^{3+}$ is known to crucially influence optical properties. In light of this, we examine the local structure around $Ce^{3+}$ in $Y_{3-x}Ce_xAl_5O_{12}$, using a combination of synchrotron X-ray and neutron scattering, neutron total scattering, X-ray absorption at the Ce K-edge, $^{27}$Al and $^{89}$Y magic angle spinning nuclear magnetic resonance, and low-temperature electron paramagnetic resonance measurements. Taken together, the different techniques confirm that the Ce is stoichiometrically incorporated in a random distribution into the structure as $Ce^{3+}$, and that is slightly expanded in its coordination polyhedron when compared with the average coordination suggested by crystal structure. The studies also point to the great rigidity of the YAG lattice, which is important for the thermal robustness of luminescence. The complementary abilities of scattering and spectroscopy to probe structural intricacies of functional materials in exquisite detail is emphasized, particularly when the features of interest occur in low concentrations.

# INTRODUCTION

The garnet host $Y_3Al_5O_{12}$, when doped with a few percent of the activator ion, $Ce^{3+}$, is a luminescent material that is almost ideally suited for excitation by a blue solid state light source. The efficiently emitted green-yellow light from the doped garnet is mixed into the incident blue from the LED, due to the garnet also providing an effective light-scattering medium. The mixed light emerges as white, and since the mid-1990s, this scheme has been at the heart of solid state white lighting.[1–4] Advantages of such light sources include their durability, long life, color stability, and their relatively benign environmental footprint, specifically in their being free of heavy metals.[5,6]

Cerium-doped YAG was first studied and proposed for use in displays by Blasse and Bril in 1967.[7] Later, when bright-blue InGaN sources first became available,[8] YAG:Ce was used for the generation of white light *via* partial down-conversion due to its favorable optical characteristics, including appropriate matching of its excitation spectrum to blue InGaN sources, high efficiency, and an emission spectrum in the complementary (to blue) color region. The absorption peaking around 460 nm and emission peaking around 540 nm are known to occur from the transition of $Ce^{3+}$ between the Ce $[Xe]4f^15d^06s^0$ ($^2F_{5/2}$, $^2F_{7/2}$) and $[Xe]4f^05d^16s^0$ ($^2D_{3/2}$, $^2D_{5/2}$) states.[9] The energy gap between these two states is significantly increased from the isolated ion by crystal field splitting of $Ce^{3+}$ $5d$ states when the $Ce^{3+}$ ion replaces the smaller $Y^{3+}$ ion in the YAG structure.[10] YAG:Ce is known to be extremely bright, with quantum efficiencies at room temperature exceeding 85%.[11] Although the reason for the blue absorption and yellow emission is well known, the crystal-chemical reasons for such high quantum efficiency in YAG:Ce have yet to be elucidated, as are the reasons for the thermal robustness of the luminescence.[12]

The optical properties of YAG:Ce have been well studied. For example, zero-phonon lines from low-temperature spectroscopy were correlated with lattice phonon energies, and characteristics of the crystal-field splitting of the $4f$ and $5d$ states of Ce in YAG were identified from the same low-temperature spectroscopy.[13] Temperature effects on the luminescence of YAG:Ce have also been investigated. At temperatures above 100 °C (especially for higher Ce concentrations) efficiency losses due to thermal quenching results in a 5% loss in quantum efficiency;[12] as temperature and/or Ce concentration is increased, the loss of efficiency with increasing temperature becomes more dramatic. Early studies of Ce concentration on the optical properties of YAG:Ce found red-shifts in the excitation and emission maxima with increasing Ce concentration.[14] A kinetic model was later developed to describe the concentration-dependent efficiency of YAG:Ce.[15] More recently, Setlur and Srivastava examined the optical characteristics of YAG:Ce, finding that lower-energy $Ce^{3+}$ sites may be present in YAG:Ce with relatively high Ce concentrations of around $x = 0.09$ in $Y_{3-x}Ce_xAl_5O_{12}$.[16] The lower-energy Ce sites lead to a red-shift in emission, and are attributed to either Ce-Ce pairs and/or Ce in perturbed lattice sites.

Among the studies that have examined structure-property relationships in luminescent garnets one study correlated emission and excitation wavelength to the average structure of the active site in garnets.[17] Synchrotron X-ray total scattering has been utilized to investigate the local structure of YAG:Ce nanoparticles,[18] and another study on $Gd^{3+}$-substituted YAG:Ce nanoparticles used Cu-k$\alpha$ X-ray diffraction to correlate the red shift of the emission with to the crystal structure.[19] One recent study looked at the local structure of the $Ce^{3+}$ ion using Ce K-edge EXAFS, and found that the nearest 8 Ce–O distances are slightly larger than the Y–O distances in YAG:Ce by about 3% in $Y_{2.97}Ce_{0.03}Al_5O_{12}$, but did not see any significant expansion of the lattice past the first three coordination shells around Ce.[20] The local structure of Ce in YAG has also been studied through first principles methods, such as one study which predicted a 3% expansion of the nearest 4 Ce–O bonds, but only a 0.03% expansion of the next-nearest 4 Ce–O bonds when compared to the undoped material.[21] Another ab-initio study examined the local structure of $Ce^{3+}$ in YAG, and predicted that the local Ce–O distances should expand by about 1% to 2% in $Y_{2.875}Ce_{0.125}Al_5O_{12}$.[22] This study also found that the expansion around Ce is observable and decreases in magnitude out to the 5th coordination shell.

In light of the great importance of this material, and the challenges associated with the careful structural analysis of small substituents in crystalline materials, we have employed a suite of powerful state-of-the-art structural probes, focusing on the local structure of the Ce ion and its interaction with the YAG host structure. The scattering and spectroscopic techniques used here yield powerful insights regarding the optical properties of YAG:Ce. More generally, these techniques enable precise structural analysis of a dopant ion at a very small concentration of around 1 mole percent. Such analysis is useful not only when investigating phosphor materials, but also when investigating other import materials with small doping amounts, such as heterogeneous catalysts, semiconductors, thermoelectrics, and luminescence up-conversion materials. With recent advances in synchrotron X-ray[23] and neutron powder diffraction[24] techniques, structural information from inorganic materials can be garnered with unprecedented accuracy. Recently developed Monte Carlo simulation techniques enable detailed statistical investigation of total neutron scattering data,[25–27] which to date has not been used on phosphor materials. X-ray absorption near edge structure (XANES) and extended X-ray absorption fine structure (EXAFS) yield crucial complementary information about the oxidation state and local structural environments of the $Ce^{3+}$ ion. High-resolution solid-state magic-angle spinning nuclear magnetic resonance (MAS NMR) and electron paramagnetic resonance (EPR) provides information complementary to scattering measurements on the local structure of $Ce^{3+}$. In particular, we demonstrate the usefulness of the paramagnetsm of $Ce^{3+}$ as an internal contrast reagent in the NMR studies. This broad range of techniques enables a new understanding of the local structure of Ce in YAG, and not only sheds new light on a well-known material, but also is expected to enhance the rational design of new phosphor materials.

# MATERIALS AND METHODS

**Sample preparation.** Samples of $Y_{3-x}Ce_xAl_5O_{12}$ with $x = 0$, 0.02, 0.04, 0.06, 0.08, and 0.09 were prepared using conventional solid-state preparation methods.[28,29] Starting materials consisting of stoichiometric amounts of $Y_2O_3$ (Sigma-Aldrich, 99.9 %), $Al_2O_3$ (Sumitomo AKP-50, >99.99 %), and $CeO_2$ (Cerac, 99.9 %), with 5% by mass $BaF_2$ (Sigma-Aldrich, 99.9 %), and 0.5% by mass $NH_4F$ (Sigma-Aldrich, 99.99 %) as sintering agents (flux), were ground in an agate mortar and pestle, placed in alumina crucibles, and fired at 1500 °C for 5 hours in an alumina tube furnace under 0.2 l/min 5 % $H_2/N_2$ gas flow. The amounts of flux and Ce were optimized by the emission intensity, resulting in optimum values of 5 mass % $BaF_2$, 0.5 mass % $NH_4F$, and a Ce concentration of $x = 0.06$ ($Y_{2.94}Ce_{0.06}Al_5O_{12}$). The quantum efficiency of the optimized sample was determined to be 87 %. Samples for XANES/EXAFS and total neutron scattering ($Y_{2.91}Ce_{0.09}Al_5O_{12}$) were prepared with stoichiometric amounts of $Y_2O_3$ (Sigma-Aldrich, 99.9 %), $Al_2O_3$ (Sumitomo, 99.9 %), and $CeO_2$ (Cerac, 99.9 %), which was ground in an agate mortar and pestle, pressed into pellets, placed in alumina crucibles on a bed of sacrificial powder, and fired at 1600 °C for 96 hours in an alumina tube furnace under 0.2 l/min 5 % $H_2/N_2$ gas flow. After the starting materials had been reacted, the phosphor cakes were ground with an agate mortar and pestle into fine powders.

**Synchrotron X-ray and neutron scattering.** High-resolution synchrotron powder diffraction data were collected using the 11-BM beamline at the Advanced Photon Source (APS) at Argonne National Laboratory, using an average wavelength of $\lambda = 0.412154$ Å. Other details regarding the experimental setup can be found elsewhere.[23]

Neutron powder diffraction was performed on the HIPD and NPDF instruments at the Los Alamos Neutron Science Center at Los Alamos National Laboratory. Powder samples were placed in vanadium cans, and time-of-flight neutron data was collected at 295 K on the HIPD instrument from 8 detector banks at ±14°, ±40°, ±90° and ±153° $2\theta$. For the

NPDF measurements, powder samples were placed in vanadium cans, and time-of-flight neutron data were collected at 15 K and 295 K from 4 detector banks at 14°, 40°, 90° and 153° $2\theta$.

Crystal structures were refined using the programs XND[30] and the EXPGUI front end for the refinement program General Structure Analysis System (GSAS).[31] Simultaneous refinements to the X-ray and neutron scattering data were completed by adjusting the profile shapes and unit cells during the LeBail fits, refining neutron absorption coefficients, instrument parameters, and the backgrounds (10-term Chebyshev polynomial function), then refining the atomic positions, and finally the atomic displacement parameters and Y/Ce occupancies. For joint X-ray and neutron refinements, the neutron data was weighted to be 1.2 times that of the X-ray data. When completed, all available structural parameters were allowed to refine simultaneously. Crystal structures were visualized using the software VESTA.[32]

**Neutron total scattering and Reverse Monte Carlo (RMC) simulations.** Time-of-flight (TOF) total neutron scattering on $Y_{2.91}Ce_{0.09}Al_5O_{12}$ was carried out at 295 K on the NPDF instrument at the Los Alamos Neutron Science Center at Los Alamos National Laboratory. The data were extracted using PDFGETN,[33] with $Q_{max} = 31$ Å. The uncertainty from the PDF measurement is around 0.1 Å ($\Delta r = \pi/Q_{max}$).[34] PDFGUI was used to fit a symmetric model to the PDF out to 50 Å.[35] Reverse Monte Carlo simulations were run using RMCPROFILE version 6 and a $4 \times 4 \times 4$ supercell with 10240 atoms.[36,37] These simulations were simultaneously constrained by the S($Q$) Bragg profile and the G($r$). All atom–atom distances were subject to a hard-sphere cutoff at 1.576 Å. Ce and Y atoms were allowed to exchange positions with a 5% chance of each move being an atom swap. Eight runs were averaged for better statistics, and simulations were run for a total of approximately 915 MC sweeps.

**X-ray absorption near edge structure (XANES) and extended X-ray absorption fine structure (EXAFS) measurements.** Ce K-edge X-ray absorption (XAS) studies were carried out at sector 20-ID beamline at the Advanced Photon source at 295 K.[38] The fifth harmonic of the undulator was used along with full scanning of the undulator. The incident beam was monochromatized using a pair of Si (311) crystals. Higher order harmonics were suppressed by detuning the monochromator to reduce the incident X-ray intensity by approximately 15%. Argon-filled ion chambers were used for the Io, It, and Iref detectors. A cold pressed pellet of $CeO_2$ in BN was placed between It and Iref to provide internal calibration for the alignment of edge position. The Ce K-edge in the $x = 0.09$ YAG:Ce sample was measured on a pure pellet of the sample in fluorescence geometry using a 13-element energy dispersive germanium detector, operated at a total count rate of $\sim$80 KHz per element. The Y background fluorescence signal impinging the Ge detector was selectively reduced by using several layers of thin aluminum foil, and care was taken to account for dead-time associated with saturation of the detector.

The $CeO_2$ absorption edge was calibrated to 40.473 keV as previously measured.[39] Simulations of the data were performed using the ARTEMIS code,[40] with fits performed in the $k^2$ regime; fits in other $k^x$ regimes gave results in good agreement with the $k^2$ regime. The $k$-space range was 2.77 $\text{Å}^{-1}$ to 16 $\text{Å}^{-1}$, giving a spacial resolution of about 0.1 Å. Ten variables were used with an estimated 25 independent points.

**Solid-state $^{27}$Al and $^{89}$Y Nuclear Magnetic Resonance (NMR) spectroscopy.** High-resolution solid-state $^{27}$Al and $^{89}$Y magic-angle spinning (MAS) NMR spectroscopy was used to investigate the local structure of YAG:Ce. The single-pulse and $T_1$-filtered $^{27}$Al NMR experiments were performed at 295 K on a Bruker AVANCE IPSO NMR spectrometer, with an 18.8 T narrow-bore superconducting magnet, operating at a frequency of 208.52 MHz for $^{27}$Al nuclei, which are 100% naturally abundant. A Bruker 3.2 mm H-X-Y triple-resonance MAS probe head was used with zirconia rotors and Kel-F® caps, with a

MAS rate of 24 kHz. The radio frequency (RF) pulse length of 2.7 $\mu$s and power level were calibrated to achieve a 15 ° ($\pi/12$) rotation of the net $^{27}$Al magnetization to ensure quantitative measurements,[41] and were calibrated with respect to the longitudinal spin-lattice relaxation time ($T_1$) to ensure the spectra were fully quantitative (recycle delay of 40 s). An external AlN sample was used as a spin-counting standard, which confirmed 100 % visibility of all $^{27}$Al nuclei in all samples. Chemical shifts were referenced to 1 M Al(NO$_3$)$_3$ at 0 ppm.

High-field measurements were recorded on a Bruker Avance III 1 GHz spectrometer operating at a $^{27}$Al Larmor frequency of 260.7 MHz. A 1 M aqueous solution of Al(NO$_3$)$_3$ was used as the chemical shift reference. The spectra of the YAG:Ce material was acquired with a 1.3 mm HX probe at 60 kHz (MAS). The $T_1$ relaxation time constants were measured using a saturation-recovery experiment comprising a saturation sequence of 30 pulses separated by delays of 3 ms, and a recovery delay taking 27 values varying from 0 to 150 s. The 1D spectra were acquired using a one-pulse sequence with 288 scans, a recycle delay of 35 s, and an excitation pulse of 50 kHz RF field amplitude and 1.67 $\mu$s duration.

$^{27}$Al spin-lattice relaxation-time behaviors of the YAG:Ce samples were established by using complementary 1D saturation-recovery and $T_1$-filtered $^{27}$Al MAS NMR spectra. 1D saturation-recovery $^{27}$Al MAS NMR spectra were acquired for a range of times, $\tau$, between 0.05 s and 70 s on a Bruker AVANCE IPSO NMR spectrometer, with an 11.7 T wide-bore superconducting magnet, operating at a frequency of 130.28 MHz for $^{27}$Al nuclei. A Bruker 4 mm H-X-Y triple-resonance MAS probe head was used with zirconia rotors and Kel-F® caps, with a MAS rate of 14 kHz. A RF pulse length of 2.51 $\mu$s was calibrated with the power level for a 90° rotation of the net magnetization of octahedral $^{27}$Al nuclei, and a 400-pulse saturation train with 2 $\mu$s between saturation pulses was used with a 0.1 s recycle delay. The long saturation train was not rotor-synchronized, leading to a saturation of the central and satellite transitions, minimizing effects from population transfer between ±5/2 and ±3/2 to ±1/2 Zeeman levels.[42,43] 1D $T_1$-filtered $^{27}$Al MAS NMR spectra (measured on the 18.8 T NMR spectrometer) were acquired with two consecutive $^{27}$Al 90° pulses, followed by a time delay, $t_{T_1} = 15$ s, and then another $^{27}$Al 90° pulse before detection to suppress octahedral $^{27}$Al signals from species with spin-lattice relaxation times shorter than the respective $t_{T_1} = 15$ s values. The 1D $T_1$-filtered $^{27}$Al MAS NMR spectra were scaled using an appropriate constant $c > 1$ to account for decreased signal intensity due to $T_1$ relaxation effects, which allows for the remaining signals to be normalized for comparison with the single-pulse $^{27}$Al spectra.

The $^{89}$Y NMR experiments were performed at the National High Magnetic Field Laboratory in Tallahassee, Florida, on a narrow-bore Magnex 19.6 T magnet fitted with a Bruker console, operating at a frequency of 40.804 MHz for $^{89}$Y nuclei, which are 100% naturally abundant. Data were collected under conditions of 6 kHz MAS and a temperature of 295 K using a Samoson 7 mm H-X triple-resonance MAS probe head with zirconia rotors and Kel-F® caps. RF pulses with a 4 $\mu$s length were used with a recycle delay of 140 s. Chemical shifts were referenced to 1 M $YCl_3$.

Spectra were modeled using the simulation program DMFIT;[44] octahedral $^{27}$Al peaks were modeled with Gaussian peaks. Relative populations of $^{27}$Al peaks were found by fitting the largest central transition peak and the two nearest spinning sidebands for each signal, then subtracting the average integrated intensity of the two spinning sideband peaks from the integrated intensity of the central peak. The $T_1$ relaxation times of octahedral $^{27}$Al nuclei were found by fixing the peak widths and peak positions of the fit to the single-pulse $^{27}$Al data, then fitting the amplitude of the peaks for the spectra from each delay time. The integrated intensity curves were then fitted using the equation $M(t) = M_z^0(1 - e^{-t/T_1})$ with the curve fitting tool in MATLAB.

**Electron Paramagnetic Resonance (EPR) spectroscopy.** EPR spectra were collected on a Bruker X-Band EPR spectrometer ($\nu = 9.486$ GHz), equipped with a Helium flow cryostat. Samples were placed in quartz tubes, and data was acquired at temperatures ranging from

4 K to 40 K. The set of linewidths as a function of temperature of the peak at 2480 G were fit with the curve fitting tool in MATLAB. Simulations of the spectra were done using the EASYSPIN code in MATLAB,[45] with a correction included for field-dependent relaxation effects. The $g_x$ peaks were fit with Gaussian peaks using the program DMFIT.[44]

## RESULTS AND DISCUSSION

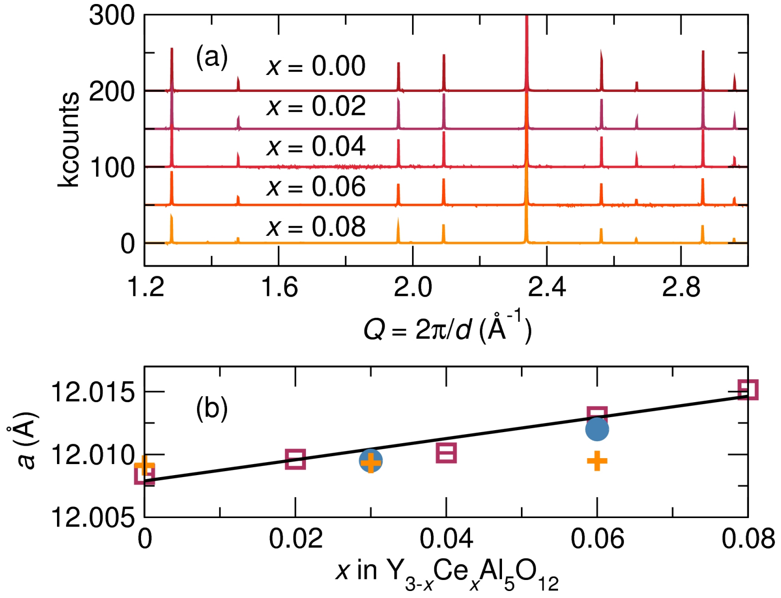

**Figure 1.** (a) Synchrotron X-ray diffraction patterns of $Y_{3-x}Ce_xAl_5O_{12}$ taken at 295 K for $x$ as indicated, and (b) the unit cell parameter from Rietveld refinement as a function of Ce concentration, $x$. The Végard law is followed, showing a very small linear expansion of the unit cell with Ce substitution. Orange plus symbols represent data from a 1979 study by Robbins et al.,[46] and filled light blue circles represent data from a study by Tien et al.[14]

**Dependence of average crystallographic structure on $Ce^{3+}$ substitution.** High-resolution synchrotron X-ray diffraction enables the study of small changes in the average structure of ordered materials, and has been used here to accurately probe the effect of the small amount of Ce substitution on the average structure of YAG. Rietveld refinements of synchrotron X-ray data of $Y_{3-x}Ce_xAl_5O_{12}$ for $x = 0$, 0.02, 0.04, 0.06, and 0.08 (data shown in Figure 1(a)) reveal a small, linear increase in the YAG unit cell lattice parameter with

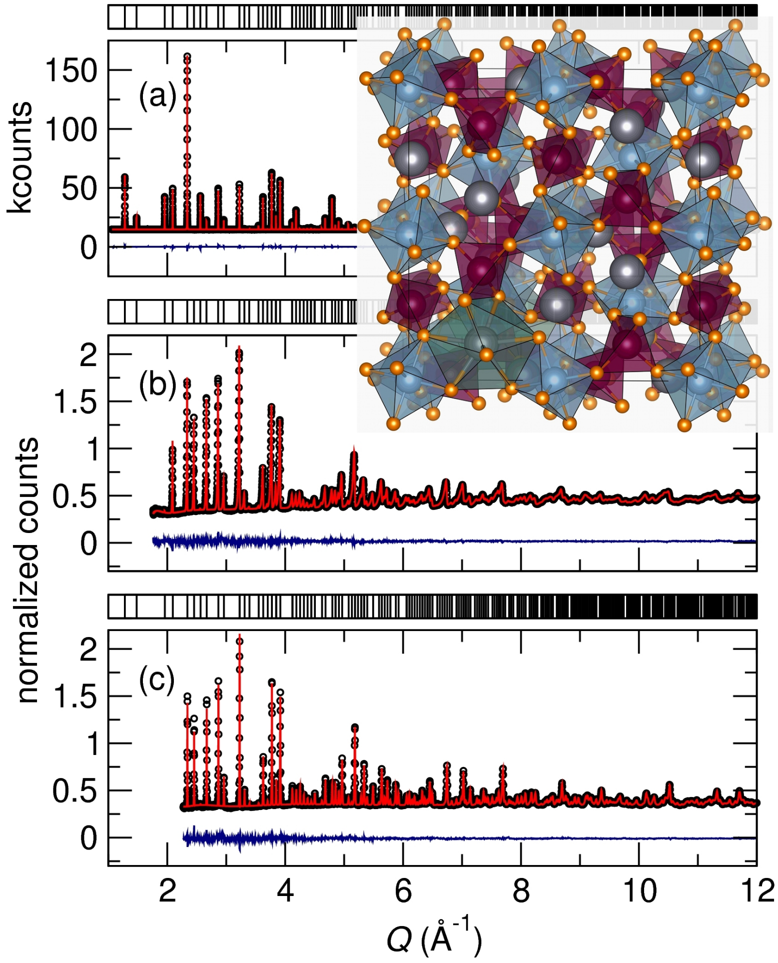

**Figure 2.** Simultaneous Rietveld refinement of (a) 11-BM synchrotron X-ray and (b) HIPD +14° detector bank neutron scattering at 295 K of $Y_{2.94}Ce_{0.06}Al_5O_{12}$, and (c) NPDF +14° detector bank neutron scattering at 15 K of $Y_{2.92}Ce_{0.08}Al_5O_{12}$. The expected peak positions are shown above each plot. The inset in the upper right shows the YAG structure looking down the *a* axis, with blue, red, grey, and orange spheres representing octahedral aluminum, tetrahedral aluminum, yttrium, and oxygen atoms, respectively.

$Ce^{3+}$ substitution as seen in Figure 1(b). Such Végard law behavior suggests all of the $Ce^{3+}$ from the starting materials is being substituted into the YAG lattice, and that the expansion of the lattice around Ce is distributed over length scales on the order of the unit cell. The change in unit cell parameter is very small, increasing by only 0.03 % from $x = 0$ to $x = 0.06$ Ce substitution in $Y_{3-x}Ce_xAl_5O_{12}$ (slope of 0.1 in Figure 1(b)). The trend found here is slightly less than a theoretically predicted increase of 0.11% from $x = 0$ to $x = 0.125$ in $Y_{3-x}Ce_xAl_5O_{12}$ (slope of 0.17).[22] A single-crystal study by Robbins et al. also found a

**Table 1. Crystallographic parameters of $Y_{3-x}Ce_xAl_5O_{12}$ from Rietveld refinement of 11-BM synchrotron X-ray, HIPD neutron, and NPDF neutron scattering data.**[a]

| T (K) | 15 | 15 | 295 | 295 | 295 |
|---|---|---|---|---|---|
| | $x = 0$ | $x = 0.08$ | $x = 0$ | $x = 0.06$ | $x = 0.09$ |
| Beamline(s) | NPDF | NPDF | 11-BM, HIPD | 11-BM, HIPD | NPDF |
| $R_p$ (%) | 1.39 | 1.41 | 6.17 (X-ray)<br>1.11 (neut.)<br>2.27 (overall) | 5.74 (X-ray)<br>1.09 (neut.)<br>2.19 (overall) | 1.49 |
| $a$ (Å) | 11.99067(2) | 11.99871(3) | 12.008476(3) | 12.013001(5) | 12.00959(4) |
| O $x$ | 0.280487(3) | 0.280487(3) | 0.280598(9) | 0.28058(1) | 0.28062(2) |
| O $y$ | 0.10103(3) | 0.10103(3) | 0.10092(1) | 0.10099(1) | 0.10094(2) |
| O $z$ | 0.19914(3) | 0.19914(3) | 0.199330(9) | 0.19946(1) | 0.19942(2) |
| refined $Ce_x$ | | 0.07(2) | | 0.09(3) | 0.10(1) |

[a] $Ce_x$ refers to the amount of Ce in $Y_{3-x}Ce_xAl_5O_{12}$. All refinements were done with the $Ia\bar{3}d$ space group (#230). The estimated standard deviations for the last significant digit are given in parenthesis.

linear increase in the YAG lattice parameter with Ce incorporation.[46] However, as shown in Figure 1, the expansion of the YAG unit cell parameter found by Robbins et al. (slope of 0.0083) is smaller than what was found here, possibly due to less Ce incorporation or resolution limitations/error in the previous study. The trend found here agrees well with another study, which found a linear increase in the unit cell of YAG with Ce incorporation, prepared using co-precipitation, with Ce substitution of up to $x = 0.18$ (slope of 0.1).[14] The conventional solid-state preparation method used here could not be substituted with more than around $x = 0.09$ with or without flux. This may be due to the low bond valence sums (BVS)[47] of Al, which are 2.7 and 2.6 for the tetrahedral ($Al_t$) and octahedral ($Al_t$) Al sites in the $x = 0$ material, respectively. As Ce is substituted into the YAG lattice, the Al–O bond distances increase, which increases the under-bonding of Al as indicated by the BVS. This may cause the YAG lattice to be unstable past a certain expansion, and may be one reason for the substitution limit of Ce in YAG.

Rietveld refinement of synchrotron X-ray and neutron diffraction data, as shown in Figure 2(a,b,c), yields unit cell parameters, the oxygen position, and Ce occupancies given in Table 1. As temperature is decreased from 295 K to 15 K, a very small contraction of about 0.15% in the unit cell and a decrease in atomic displacement parameters (ADPs) are observed. A small change in the unit cell parameter with temperature is consistent with previous measurements of the thermal expansion of YAG, which show the thermal expansion parameter, $\alpha$, to be on the order of $10^{-6}\,\mathrm{K}^{-1}$.[48] The 295 K NPDF refinement of $Y_{2.91}Ce_{0.09}Al_5O_{12}$ shows a unit cell that is smaller than expected based on Figure 1(b). Since the neutron data here was collected using time-of-flight methods, $Q$-values come from correlations to the measured time-of-flight of neutrons. This means a small difference from the calibration run to the actual sample run can occur, causing slight differences in the unit cell parameter. The least-squares fit to the PDF of the same NPDF data shows a unit cell parameter in better agreement with Figure 1(b), as discussed later in this paper. The refined occupancy of Ce from the HIPD neutron data gives a result with slightly more Ce than expected [$x$ =0.09(3) compared to the nominal $x$ =0.06] The results from the NPDF refinement for $x = 0.08$ and $x = 0.09$ are within the estimated standard deviation of the nominal values, indicating that the NPDF instrument may be slightly more sensitive to the Ce atoms in the samples than the HIPD instrument.

**Local structure around Ce$^{3+}$ from scattering.** Rietveld analysis is a powerful tool for investigating the average structure of materials, but it cannot be used to garner information on the local structure of materials since the data represents the structure of a material averaged over many unit cells. Of course, the local structure around Ce in YAG is closely related to the optical properties of YAG:Ce, since the nature of the Ce–O bonds will determine the 5$d$ energy levels, and hence, the excitation and emission energies. The PDF, which captures the local and long-range structures of materials through a sine Fourier transform of Bragg scattering, gives local structure information that is complementary to a Rietveld analysis. One way to compare the average structure from Rietveld refinement to the local structure from total neutron scattering is by fitting the PDF with a least-squares method using a periodic unit cell in PDFGUI.[35] The PDFGUI least-squares fit to the 295 K

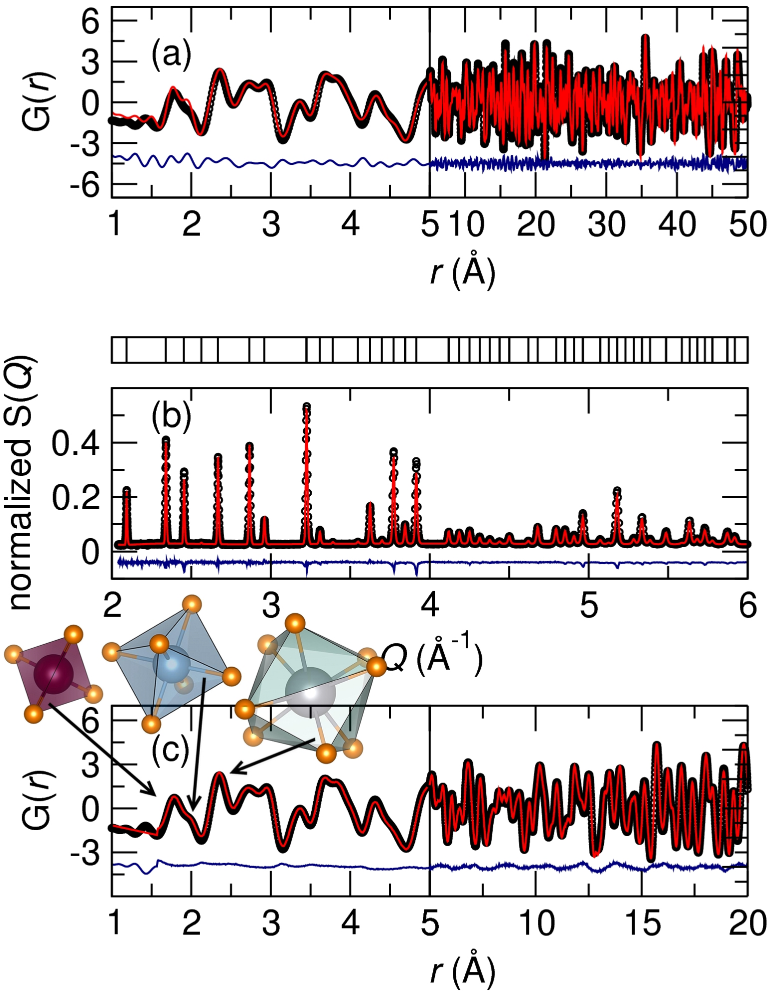

**Figure 3.** NPDF neutron data taken at 295 K with (a) PDFGUI least-squares fit of G($r$), and reverse Monte Carlo fits of (b) S($Q$) and (c) G($r$) for $Y_{2.91}Ce_{0.09}Al_5O_{12}$. The expected peak positions for S($Q$) are shown above (b). Polyhedra are shown inset above (c), with arrows denoting the corresponding peaks in the PDF for the (from left to right) tetrahedral Al, octahedral Al, and dodecahedral Y sites.

PDF of $Y_{2.91}Ce_{0.09}Al_5O_{12}$ out to 50 Å, shown in Figure 3(a), fits the data well with a $R_{wp}$ of 13.9%. The Rietveld analysis of the S($Q$) data for $Y_{2.91}Ce_{0.09}Al_5O_{12}$ ($R_{wp} = 1.49\%$) yields a cell parameter of 12.010 Å, considerably smaller than the result of 12.017 Å from a PDFGUI least-squares fit of the PDF to 50 Å, which is in good agreement with what is expected from Figure 1(c). The Rietveld unit cell is smaller likely due to the time-of-flight correlation which is fitted based on a standard material, such as silicon. This correlation can differ slightly from run to run depending on the exact sample placement, and is likely

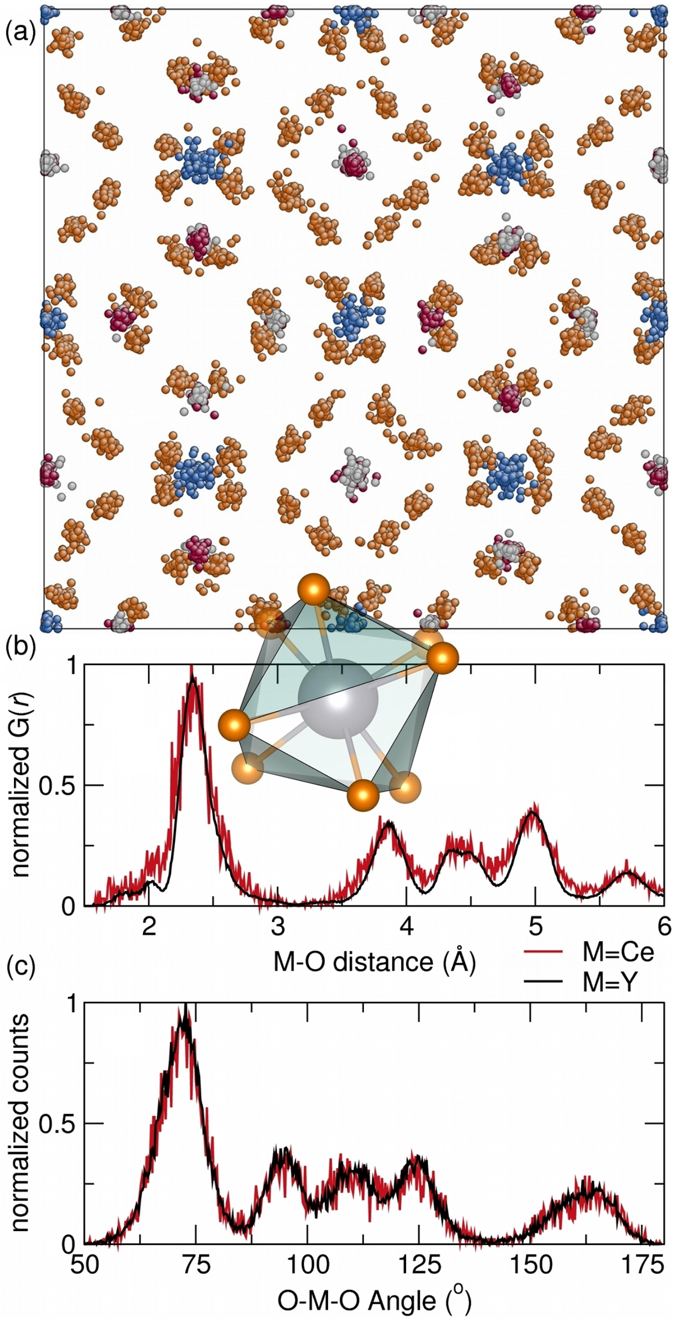

**Figure 4.** (a) View down the *a*-axis of the 4 × 4 × 4 RMC supercell of $Y_{2.91}Ce_{0.09}Al_5O_{12}$ collapsed onto a single unit cell, fit with 915 MC sweeps to NPDF neutron data collected at 295 K; (b) metal-oxygen distance distributions from the average of 8 reverse Monte Carlo fits of 295 K NPDF neutron data, and (c) oxygen–metal–oxygen bond angle distributions for Y and Ce in $Y_{2.91}Ce_{0.09}Al_5O_{12}$. The inset shows a dodecahedral Y–O polyhedron from the average YAG structure. Blue, red, grey, and orange spheres in (a) represent octahedral aluminum, tetrahedral aluminum, yttrium, and oxygen atoms, respectively.

the reason for the smaller obtained unit cell from Rietveld analysis.

The limitations of least squares refinement of PDF data using a periodic unit cell, such as symmetry constrains in PDFGUI, can be overcome by using reverse Monte Carlo (RMC) simulations, which simultaneously models the local and long-range structure of a material without symmetry constraints.[36,37,49,50] Since Y and Ce have sufficiently different neutron scattering lengths (4.03 barn and 7.15 barn for Ce and Y, respectively), Ce can be distinguished from Y in the simulations, allowing for selective investigation of the local structure around Ce in YAG. Comparison of a simulation of YAG:Ce with Y in place of Ce shows that the fit is slightly improved by using Ce instead of Y in the simulation ($\chi^2$ of 3.55 compared to 3.57 for simulations with Ce and with only Y used, respectively). The result of the RMC fits to the data are shown in Figure 3(b),(c), and the super cell of $4 \times 4 \times 4$ YAG unit cells is shown collapsed onto one unit cell in Figure 4(a).

The Ce–O and Y–O distance histograms from the RMC simulation of $Y_{2.91}Ce_{0.09}Al_5O_{12}$ in Figure 4(c) show the Ce–O distance distribution and O–Ce–O bond angle distribution are the same as the Y–O distance distribution and O–Y–O bond angle distribution. The average BVS[47,51] from the Ce–O bond distance histogram is $4.0 \pm 0.1$, much higher than the nominal valence state of 3 and the BVS of Y, which is around $3.1 \pm 0.1$. This implies that $Ce^{3+}$ is severely compressed in the YAG lattice, since the Shannon-Prewitt ionic radius of 8-coordinate $Ce^{3+}$ (1.143 Å) is much larger than radius of 8-coordinate $Y^{3+}$ (1.019 Å).[52] The compression leads to a large crystal field splitting of the Ce 5*d* states in YAG, since short Ce–O bond distances lead to large crystal field splittings.[9] This results in the blue absorption and yellow emission that has been observed, consistent with previous observations of an unusually large crystal field spitting in YAG:Ce.[10] The average Ce–O distances of 2.31 Å and 2.44 Å found here are slightly less than those from the EXAFS results as discussed later in this paper, which show the Ce–O bond distances to be 2.40(2) Å and 2.50(2) Å, but are within the error of the measurements since the uncertainty is around 0.1 Å in the PDF and EXAFS measurements. The nearly imperceptible distortion of the lattice around $Ce^{3+}$ is consistent with the small increase in unit cell parameter found from Rietveld analysis in Figure 1(b), since a larger local distortion around Ce would be expected to expand the lattice by a greater amount.

The RMC simulation results also show a random distribution of Ce–Ce distances, indicating a random distribution of Ce in the lattice. This is consistent with the $^{27}$Al NMR and EPR results, which, as discussed later in this paper, support a random distribution of Ce$^{3+}$ ions in the YAG lattice.

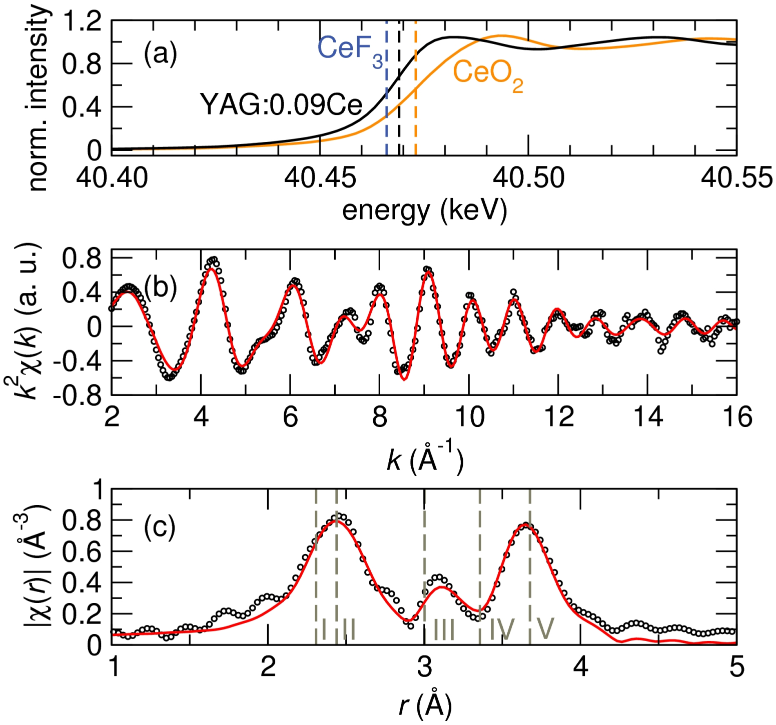

**Figure 5.** Ce K-edge (a) XANES spectra of $Y_{2.91}Ce_{0.09}Al_5O_{12}$ and $CeO_2$, (b) $k^2\chi(k)$ data and fit, and (c) $\chi(r)$ data and fit collected at 295 K. The vertical dashed lines in (a) indicate the absorption edges for $CeF_3$ at 40.466 keV,[39] $Y_{2.91}Ce_{0.09}Al_5O_{12}$ at 40.469 keV, and $CeO_2$ at 40.473 keV.[39] The vertical dashed lines in (c) indicate the Y–X (X = O, Al, Y) inter-atomic distances from Rietveld refinement of 295 K NPDF data of the same sample, with I, II, III, IV, and V corresponding to Y–O1, Y–O2, Y–$Al_t$, Y–$Al_o$, and Y–$Al_t$/Y distances, respectively. A phase shift was applied to the data and fit in (c) based on the first Ce–O coordination shell.

Total neutron scattering offers a unique way, free from symmetry constraints, to investigate the local structure around Ce$^{3+}$ in YAG:Ce, but EXAFS is an even more selective probe for investigating the local structure of Ce in YAG. Simultaneously, the oxidation state

**Table 2. Inter-atomic Ce–X distances for $Y_{2.91}Ce_{0.09}Al_5O_{12}$ from Rietveld refinement of 295 K NPDF data compared with those from the fit to 295 K 20-BM EXAFS data.**[a]

| X | $N$ | Ce–X distance (Å) | |
|---|---|---|---|
| | | Rietveld | EXAFS |
| O1 | 4 | 2.3090(2) | 2.40(2) |
| O2 | 4 | 2.4401(2) | 2.50(2) |
| $Al_t$ | 2 | 3.00238(2) | 3.05(1) |
| $Al_o$ | 4 | 3.35677(2) | 3.41(1) |
| $Al_t$ | 4 | 3.67715(2) | 3.71(1) |
| Y | 4 | 3.67715(2) | 3.71(1) |

[a] The EXAFS fit also included the next 2 coordination shells around Ce (Ce–O pairs), but the distances did not differ significantly from the Rietveld refinement. The estimated standard deviations are shown in parenthesis for the last significant digit.

of the Ce atoms in YAG:Ce has been probed with XANES. The Ce oxidation state is of utmost importance to the optical properties of YAG:Ce, since $Ce^{4+}$ ions have been known to quench $Ce^{3+}$ luminescence.[53] The XANES data collected on $Y_{2.91}Ce_{0.09}Al_5O_{12}$ at 295 K, shown in Figure 5(a), reveal that the Ce absorption edge lies at 40.469 keV, a lower energy than the Ce absorption edge in $CeO_2$ at 40.473 keV, but a higher energy than Ce in $CeF_3$ at 40.466 keV.[39] This result shows that the Ce in YAG is indeed in the 3+ state, as is crucial for the optical properties. It also confirms the $^{27}$Al NMR result that all Ce in these materials is in the 3+ state, as discussed later in this paper. The higher absorption edge of $Y_{2.91}Ce_{0.09}Al_5O_{12}$ compared to $CeF_3$ is likely due to the nature of fluoride versus oxide lattices.

A fit to the EXAFS data shown in Figure 5(b),(c) ($R$-factor of 1.55%) reveals that even with relatively high concentrations of Ce in $Y_{3-x}Ce_xAl_5O_{12}$ ($x = 0.09$ in this case), the lattice locally distorts by the same amount as was observed with lower concentrations of

Ce ($x = 0.03$) in another EXAFS study.[20] The 2 Ce–O distances of 2.40(2) Å and 2.50(2) Å agree well with previous findings of 2.38(1) Å and 2.52(2) Å[20] and the RMC results, but are slightly larger compared to the values from two theoretical studies of 2.373 Å and 2.468 Å,[22] and 2.370 Å and 2.441 Å.[21] The small 3% expansion of the Ce–O bond distances compared to the average structure Y–O distances allows the BVS[47,51] of $Ce^{3+}$ to decrease from 4.0±0.1 to 3.3±0.1. This indicates that while Ce is tightly compressed in the YAG:Ce lattice, a small expansion of the local bond lengths dramatically decreases the BVS to a more reasonable value.

The higher resolution here compared to the previous EXAFS study of YAG:Ce[20] enables a more precise investigation of the Al and Y atoms near Ce in the structure, and reveals that the Ce–Al and Ce–Y distances in the first few Ce coordination shells do in fact significantly deviate from the average structure Y–Al and Y–Y distances. This shows that the distortion around $Ce^{3+}$ ions in YAG is not limited to the first few coordination shells of O and Al atoms, but in fact spans five or more coordination shells. This is a more satisfying explanation as to why the lattice expands with addition of Ce–the distortions are not contained within a short distance, but are spread out over the structure. This 3% change in the first coordination sphere of Ce–O translates to an expansion of the unit cell on the order of 0.01% seen in the synchrotron X-ray results, due to spreading of the distortion over the YAG lattice. Past the Ce–Y coordination shell at around 3.7 Å, the distortions become imperceptible to the EXAFS measurement. However, it is anticipated from the Rietveld analysis that these distortions do exist in smaller amounts as distance from a substituted Ce ion increases.

**Table 3. Isotropic atomic displacement parameters of $Y_{3-x}Ce_xAl_5O_{12}$ from Rietveld refinement and PDFgui (least-squares fit to the PDF) fits of neutron and X-ray scattering data.[a]**

| T (K) | 15 | 15 | 295 | 295 | 295 | 295 | 295 |
|---|---|---|---|---|---|---|---|
| | $x$ =0 | $x$ =0.08 | $x$ =0 | $x$ =0.06 | $x$ =0.09 | $x$ =0.09 | $x$ =0.09 |
| data type | NPDF | NPDF | HIPD neutron<br>11-BM X-ray | HIPD neutron<br>11-BM X-ray | NPDF | NPDF<br>(1 Å to 50 Å) | |
| method | Rietveld | Rietveld | Rietveld | Rietveld | Rietveld | PDFgui | EXAFS |
| Y/Ce $B_{iso}$ (Å$^2$) | 0.16(1) | 0.20(1) | 0.178(3) | 0.227(4) | 0.36(1) | 0.43(6) | 0.36(4) |
| $Al_O$ $B_{iso}$ (Å$^2$) | 0.12(1) | 0.20(1) | 0.215(4) | 0.250(5) | 0.33(1) | 0.38(4) | 0.2(1) |
| $Al_t$ $B_{iso}$ (Å$^2$) | 0.19(3) | 0.23(2) | 0.21(1) | 0.22(1) | 0.34(2) | 0.39(2) | 0.2(1)/0.36(4)[b] |
| O $B_{iso}$ (Å$^2$) | 0.25(1) | 0.30(1) | 0.255(5) | 0.295(6) | 0.43(1) | 0.51(6) | 0.36(4) |
| $\theta_D$ (K) | 634 | 506 | 853 | 760 | 628 | 578 | 690 |

[a] All refinements used the $Ia\bar{3}d$ space group (#230). The numbers reported for the EXAFS fit are mean-square relative displacement factors. The Debye temperatures shown, $\theta_D$, are the average of the values calculated from the isotropic atomic displacement parameters.[54] The anisotropic displacement parameters can be found in the supporting information, Table S1. Estimated standard deviations for the last digits of parameters are given in parenthesis.

[b] The two atomic displacement parameters are for the 3rd and 5th coordination shells around Ce, respectively.

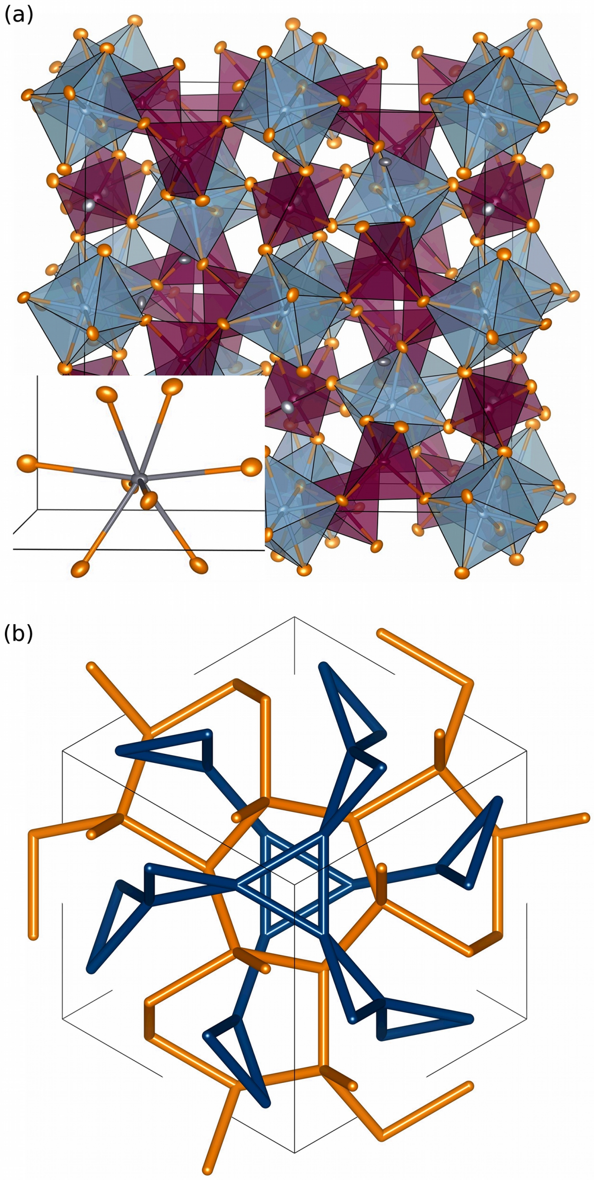

**Figure 6.** (a) View down the *a*-axis of the Rietveld-refined structure of $Y_{2.94}Ce_{0.06}Al_5O_{12}$ at 295 K from 11-BM synchrotron X-ray data and HIPD neutron data, with the inset showing an expanded view of a Y atom with bonds drawn to the surrounding O atoms. 99% probability atomic displacement parameters are shown by blue, red, grey, and orange ellipsoids, which represent octahedral aluminum, tetrahedral aluminum, yttrium, and oxygen atoms, respectively. (b) View down the (111) face of the YAG unit cell, showing the inter-penetrating networks of Y and Al, which form a double-gyroid structure. The blue cylinders are drawn between Y atoms, while the orange cylinders connect tetrahedral Al atoms. The octahedral Al atoms were excluded from (b) for clarity.

**The rigid YAG lattice is related to its high quantum efficiency.** Whereas the X-rays used earlier in this paper to accurately determine the unit cell have a form factor that decays rapidly with increasing $Q$, neutron scattering intensities essentially remain flat with increasing $Q$, enabling a precise investigation of the atomic displacement parameters.[55] A simultaneous Rietveld refinement of synchrotron X-ray and neutron scattering therefore yields a structural model of a material that accurately represents the long-range order and ADPs. Rietveld fits of only synchrotron X-ray data tended to give smaller ADPs, while fits using only neutron data gave slightly larger ADPs. The joint refinements used here gave ADPs that were approximately the average of the ADPs from either neutron or synchrotron X-ray data. As shown in Table 3, increasing Ce concentration correlates with increasing ADPs. This is due to greater static disorder in the structure from distortions from the substituted Ce ions, as well as an increase in the low-frequency phonon modes due to the addition of heavier Ce atoms into the structure. The least-squares PDFGUI fit to the PDF out to 50 Å gives larger isotropic ADPs than the Rietveld fit, which is due to the inclusion of the local and long-range structures in the same refinement.

We hypothesize that the small ADPs from Table 3 are related to the high quantum efficiency of YAG:Ce of around 90 %. The ADPs found here, shown for the unit cell from $Y_{2.94}Ce_{0.06}Al_5O_{12}$ with 99% probability in Figure 6(a), are slightly less than those of yttrium-aluminum perovskite[56] and $MgAl_2O_4$,[57] and about half of those of cerium-aluminum perovskite.[58] The small ADPs indicate a high degree of crystalline order and small thermal motions of atoms, and decrease with decreasing temperature as expected. This coincides with the increase of quantum efficiency at low temperature,[12] supporting the relationship between small ADPs and high quantum efficiency. The mean-square relative displacements (MSRDs) from the EXAFS fit are much smaller than the ADPs found from Rietveld analysis of the same sample; the ADPs from Rietveld and MSRDs of the EXAFS converge as the distance from Ce increases. Of course, caution must be taken when comparing ADPs to MSRDs, since the MSRDs include correlated atomic motions. The small MSRDs from the EXAFS fit are the result of the large size of Ce in the lattice, which diminishes the amount of space available for nearby atoms to vibrate.

The tight compression of Ce in YAG found from the RMC and EXAFS results, and the small MSRDs near Ce are related to the low probability of non-radiative transitions and high quantum efficiency of YAG:Ce. Small MSRDs around substituted Ce ions decrease the accessible phonon energy levels that aid in quenching excited $Ce^{3+}$ electrons non-radiatively, thereby decreasing the probability of non-radiative transitions.[9] A relationship between high quantum efficiency and small ADPs is also supported by the Debye temperature. The relationship between Debye temperature ($\theta_D$), which gives an estimate of the temperature at which the highest frequency vibrational mode of a crystal is excited,[54] and the average atomic displacement shows how less phonon modes are accessible at a given temperature in a rigid lattice compared to a floppy lattice. For example, the average $U_{iso}$ measured here for YAG at 295 K is around 0.0093 $\text{Å}^2$ , corresponding to the previously measured $\theta_D = 760\,\text{K}$.[59] Another crystal structure, $KGd(WO_4)_2$, with a lower $\theta_D$ of 580 K,[59] has an average $U_{iso}$ measured as 0.020 $\text{Å}^2$,[60] indicating that at a given temperature, a higher proportion of phonon modes will be populated in $KGd(WO_4)_2$ compared to YAG.

The isotropic ADPs can in fact be used to calculate the Debye temperature,[54] and as shown in Table 3, the Debye temperatures calculated in this fashion are typically less than the literature value of 760 K in the low-temperature limit, and greater than the literature value in the high-temperature limit. The high temperature limit involves an assumption that the measurement temperature is greater than $\theta_D$, which is not valid in our case and explains the discrepancy. The low-temperature limit result for $x = 0$ is much less than the reported value of 760 K, which agrees with the typical trend of results for other crystal structures in literature,[61] but may also be due to static disorder in the samples and the substutution of Ce for Y. As Ce is added to the lattice, $\theta_D$ decreases, indicating that more vibrational modes are accessible at a given temperature. This is consistent with the larger mass of Ce, which is expected to increase the number of low-frequency Einstein modes available to the system. Non-radiative transitions, which decrease the quantum efficiency, can occur due to vibronic coupling and other phenomena associated with disorder and large amounts of vibrations near activator ions.[9] The decreasing $\theta_D$ should therefore correlate with an increase of non-radiative transitions and decreased quantum efficiency. Till now, a decrease in quantum efficiency with increasing activator ion concentration has been attributed to energy transfer between activator ions, but appears to also result from an increased amount of accessible phonon modes at a given temperature. The smaller MSRDs from the EXAFS fit result in an even smaller calculated $\theta_D$ compared to the $\theta_D$ from Rietveld refinement ADPs, indicating that Ce locally sees a higher Debye temperature. This decreases the non-radiative recombination pathways of a $Ce^{3+}$ ion in the excited state, further supporting the relationship between small ADPs/MSRDs and high quantum efficiency in phosphors.

The rigid lattice exhibited by YAG is of course closely related to its structure. The Y–Y and Al–Al connectivity forms a double-gyroid structure though Y–O–Y and $Al_t$–O–$Al_O$–O–$Al_t$ pathways, shown as a simplified version of Y–Y and $Al_t$–$Al_t$ connectivities in Figure 6(b). The $Al_t$ and $Al_O$ network is formed by corner sharing of the Al polyhedra, which would not typically happen with something with a higher charge and similar coordination numbers, such as tetrahedral Si, per Pauling's fourth rule of determining the structure of ionic crystals.[62] The high connectivity of the YAG lattice decreases the degrees of freedom available for phonon modes, especially local Einstein-like modes, leaving few vibrational modes to aid in non-radiative transitions of the unpaired $Ce^{3+}$ electron from the excited $5d$ to the $4f$ ground state.

**Probing the local structure around $Ce^{3+}$ by its paramagnetic effects on proximal $^{27}$Al and $^{89}$Y nuclei.** Structural reasons for the high quantum efficiency of YAG:Ce have also been investigated here by spectroscopic methods, which offer a means to probe materials in a way that is complementary to scattering methods. For example, solid-state NMR spectroscopy can be used to accurately quantify nuclei by phase or crystallographic site in a material, which can be compared to results from scattering. NMR also enables selective

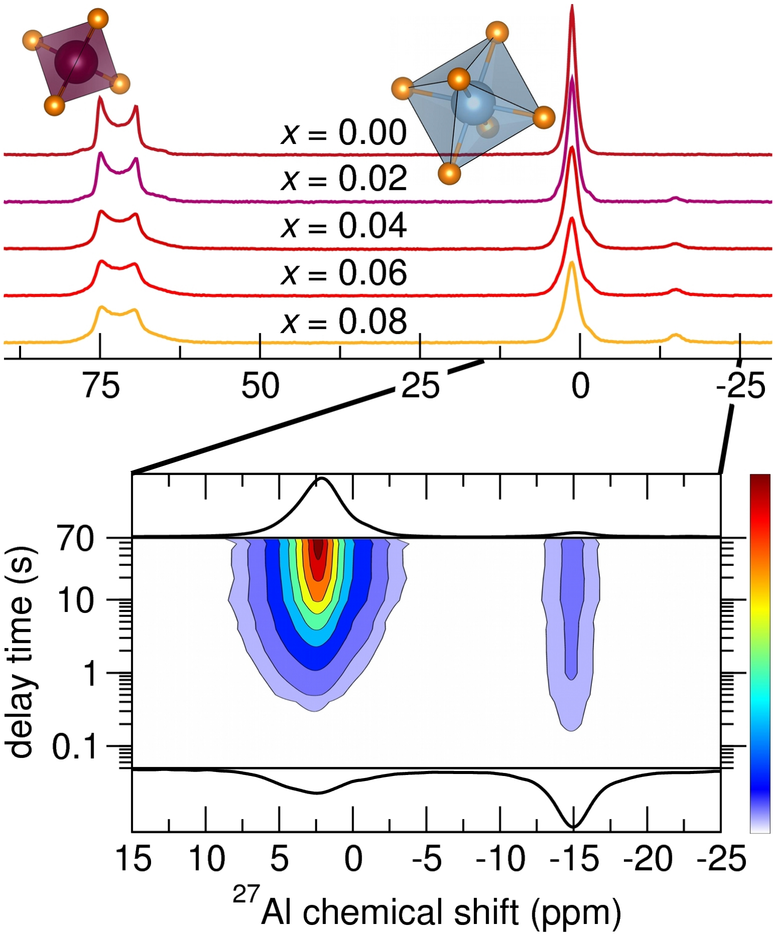

**Figure 7.** (a) Single-pulse solid-state $^{27}$Al NMR spectra (24 kHz MAS) of $Y_{3-x}Ce_xAl_5O_{12}$ taken at 295 K and 18.8 T with varying amounts of $Ce^{3+}$ substitution in $Y_{3-x}Ce_xAl_5O_{12}$ as indicated. The small signal near $-15$ ppm is from octahedral $^{27}$Al nuclei near substituted Ce. (b) Solid-state $^{27}$Al NMR saturation recovery spectra (14 kHz MAS) on the octahedral $^{27}$Al signals of $Y_{2.94}Ce_{0.06}Al_5O_{12}$ at 295 K and 11.7 T, showing that the $-15$ ppm signal saturates much faster (has a shorter $T_1$ relaxation time) than the bulk octahedral signal. Contour lines are at relative intensity levels of 0.1, 0.2, 0.5, 1, 1.5, 2.0, 2.5, 3.0, and 3.3.

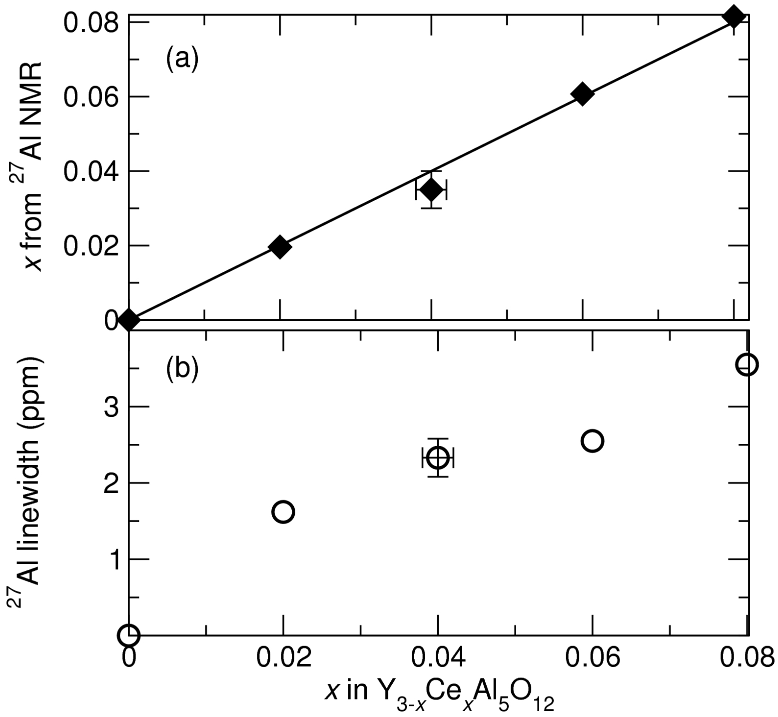

**Figure 8.** (a) Cerium composition in $Y_{3-x}Ce_xAl_5O_{12}$ as calculated from fits to 1D single-pulse solid-state $^{27}$Al MAS NMR spectra and (b) FWHM ($\Gamma$, open circles) from the same fits. The line in (a) is the $y = x$ line of Ce composition, $x$. Ce concentration, $x$, was found from the fits by taking the relative integrated intensity of the octahedral $^{27}$Al compared to the entire octahedral $^{27}$Al region and dividing by 4 (for the number of $^{27}$Al nuclei in the first coordination shell around Ce), and multiplying by 3 to normalize for the nominal composition, $Y_{3-x}Ce_xAl_5O_{12}$.

investigation of the local electronic environment of one particular nucleus, while conventional scattering methods must probe all atoms in a material at once. In YAG:Ce, the 100% naturally abundant $^{27}$Al and $^{89}$Y nuclei enable such a selective and quantitative analysis that provides unique information complementary to the scattering and XANES/EXAFS results. The unpaired electron in the $4f$ shell of $Ce^{3+}$ alters the local magnetic field of nearby nuclei, enabling a selective probe of the YAG lattice around the $Ce^{3+}$ dopant ions. The 1D single-pulse $^{27}$Al spectra in Figure 7(a) of $Y_{3-x}Ce_xAl_5O_{12}$ with $x = 0$, 0.02, 0.04, 0.06, and 0.08, shows the resolved $^{27}$Al signals located at 77 ppm and 1.3 ppm, associated with the tetrahedral and octahedral $^{27}$Al sites, respectively. These results confirm that the samples are highly crystalline and single-phase, and are in good agreement with previous measurements of undoped YAG.[63–65] As Ce is added, broadening of both signals is observed, and a second octahedral signal appears near $-15$ ppm. The relative integrated signal intensities of the two types of $^{27}$Al signals from all samples agree well with the expected 3:2 ratio for the tetrahedral:octahedral $^{27}$Al nuclei in YAG, including the signal near $-15$ ppm in the octahedral $^{27}$Al population. The signal near $-15$ ppm has been previously regarded as an impurity,[66] but is in fact the signal from the first coordination sphere of $^{27}$Al nuclei near paramagnetic $Ce^{3+}$ in YAG:Ce. Such a peak assignment is supported by a linear increase of the integrated intensity with increasing Ce concentration, as shown in Figure 8. This has never before been reported in cerium-doped YAG, though displacement and broadening of $^{27}$Al and $^{89}$Y NMR spectra due to substitutions of rare-earth ions has been observed in the past in YAG:Tb,[67] stannates,[68] and pyrochlores.[69] Materials prepared with or without $BaF_2$ and $NH_4F$ fluxes yielded nearly identical 1D single-pulse solid-state $^{27}$Al MAS NMR spectra as shown in supporting information Figure S2(a), showing that the local environment of Ce is not affected by the use of $BaF_2$ and $NH_4F$ flux in the preparation of the YAG:Ce materials. This observation suggests Ba does not substitute into the lattice in substantial amounts, consistent with the large energy (from DFT calculations) associated with Ba substitution on the Y site of around 5 eV.[70]

**Table 4. Ce–X distances from the HIPD/11-BM 295 K Rietveld refinement, with parameters from fits to the $^{27}$Al and $^{89}$Y NMR spectra for $Y_{2.94}Ce_{0.06}Al_5O_{12}$.[a]**

| | Coord. | Number | Ce–X | Calculated | Fitted | $\Gamma$ | | Population |
|---|---|---|---|---|---|---|---|---|
| Atom | shell | of nuclei | $r$ (Å) | $\delta_{iso}$ (ppm) | $\delta_{iso}$ (ppm) | (ppm) | $T_1$ (s) | (%) |
| 6-coord. | bulk | | | | 1.26 | 2.14 | 6.55 | 71.5 |
| $^{27}$Al | 1 | 2 | 3.36 | −27.2 | −15.0 | 2.52 | 0.318 | 4.25 |
| | 1 | 2 | 3.36 | 21.6 | −15.0 | 2.52 | 0.318 | 4.25 |
| | 2 | 2 | 5.41 | 6.1 | 3.15 | 2.12 | 2.44 | 4.0 |
| | 2 | 2 | 5.41 | 1.7 | bulk[b] | bulk[b] | | |
| | 3 | 4 | 6.88 | −1.7 | −1.18 | 2.29 | 5.82 | 7.9 |
| | 3 | 4 | 6.88 | 2.3 | 3.15 | 2.12 | 2.44 | 8.1 |
| 4-coord. | bulk | | | | 77 | | | 86.9 |
| $^{27}$Al | 1 | 2 | 3.00 | 105.4 | 108[c] | | | |
| | 2 | 2 | 3.68 | 61.5 | 70.5 | | | 3.4 |
| | 2 | 2 | 3.68 | 84.7 | 70.5 | | | 3.4 |
| | 3 | 2 | 5.62 | 80.4 | bulk[b] | | | |
| | 3 | 2 | 5.62 | 73.0 | bulk[b] | | | |
| | 3 | 4 | 5.62 | 77.7 | bulk[b] | | | |
| $^{89}$Y | bulk | | | | 222 | 2.6 | | 67.0 |
| | 1 | 2 | 3.68 | 206 | 237 | 2.9 | | 5.5 |
| | 1 | 2 | 3.68 | 229 | 237 | 2.9 | | 5.5 |
| | 2 | 2 | 5.62 | 225 | 225 | 2.1 | | 5.5 |
| | 2 | 2 | 5.62 | 218 | 212 | 2.0 | | 11.0 |
| | 2 | 4 | 5.62 | 223 | bulk[b] | | | |
| | 3 | 2 | 6.00 | 226 | 225 | 2.1 | | 5.5 |

[a] The calculated paramagnetic displacement ($\delta_{iso}$) was obtained from Equation 1, fitted displacements of octahedral/tetrahedral $^{27}$Al and $^{89}$Y, FWHM ($\Gamma$), and populations are from fits to the data using DMFIT, and $T_1$ relaxation times were measured from saturation-recovery experiments. The octahedral $^{27}$Al peaks were modeled with Gaussian peaks.

[b] "Bulk" indicates the signal was assumed to coincide with the bulk signal.

[c] The fitted value is from the 23.5 T spectra in Figure 10.

Calculation of the Ce concentration from the relative integrated intensities of the $-15$ ppm signal shown in Figure 8(a) reveals a linear increase in the amount of octahedral $^{27}$Al nuclei in the first coordination sphere around substituted Ce, which matches the nominal compositions. This indicates that all the Ce in the starting materials has been incorporated into the YAG lattice, in agreement with the 11-BM synchrotron X-ray Rietveld refinement results, which showed linear expansion of the unit cell with Ce incorporation. Additionally, for the displacement of the octahedral $^{27}$Al NMR signal to occur, Ce must be in the 3+ state so that it is paramagnetic. Therefore, the quantitative results in Figure 8(a) also demonstrate that all of the Ce in the lattice must be in the 3+ state, corroborating the XANES result. The full width at half maximum ($\Gamma$) values in Figure 8(b) show a linear increase with Ce content, indicating a larger amount of inhomogeneity in the local electronic environment of the octahedral $^{27}$Al nuclei nearest Ce with increasing Ce substitution. Finally, since the paramagnetic displacement of the signal from octahedral $^{27}$Al sites near Ce$^{3+}$ is additive with the amount of proximal Ce$^{3+}$ ions, a $^{27}$Al nucleus bordering two Ce$^{3+}$ ions would resonate around $-30$ ppm.[68,69,71] The signal around $-30$ ppm from such $^{27}$Al nuclei is only discernible from the noise in the spectrum of the $x = 0.08$ material since the relative population of this peak is very small. Quantification of the spectra from the $x = 0.08$ material results in about 0.44% of octahedral Al in the material being found near 2 Ce$^{3+}$ ions, in good agreement with the 0.40% expected in a random distribution of Ce$^{3+}$ in the lattice. This result agrees well with the RMC result, which showed a random distribution of Ce in the YAG lattice.

The displacement of octahedral $^{27}$Al signals due to proximal Ce$^{3+}$ ions is a result of through-bond sharing of the Ce$^{3+}$ $4f$ electron spin density with the surrounding lattice (the Fermi "contact" shift) and/or a through-space dipolar interaction ("pseudocontact" shift) between the unpaired Ce$^{3+}$ $4f$ electron with the $^{27}$Al unpaired nuclear spins.[69,72] The equation for fractional displacement in nuclear resonance frequency due to the dipolar contribution is[71]

$$\frac{\Delta\nu}{\nu_0} = \frac{-g^2\beta^2 J(J+1)(2J-1)(2J+3)F}{60(kT)^2 r^3}, \tag{1}$$

where

$$F = A_2^0 \left\langle r^2 \right\rangle (3cos^2\theta - 1) \left\langle J \,\|\, \alpha \,\|\, J \right\rangle. \tag{2}$$

The angular factor, $F$, assumes axial symmetry of the lanthanide site. The terms $g = 6/7$, $J = 5/2$, and $\langle J \,\|\, \alpha \,\|\, J \rangle = -0.0571$ are constants specific to $\mathrm{Ce}^{3+}$.[71] The value $A_2^0 = -159\,\mathrm{cm}^{-1}$ is a crystal field parameter for $\mathrm{Ce}^{3+}$ in YAG,[73] and the value of $\left\langle r^2 \right\rangle$ for the $\mathrm{Ce}^{3+}$ $J = 5/2$ state is 1.193 (in atomic units).[74]

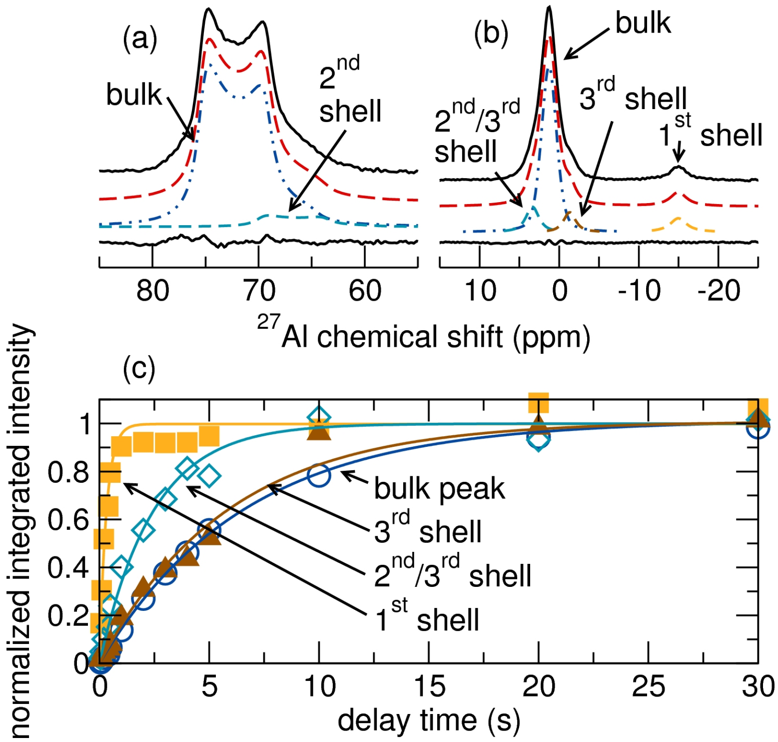

**Figure 9.** Fits to the (a) tetrahedral and (b) octahedral components of the 1D single-pulse solid-state $^{27}$Al NMR spectra (24 kHz MAS) of $\mathrm{Y_{2.94}Ce_{0.06}Al_5O_{12}}$ taken at 295 K and 18.8 T. The fits have been offset from the data for clarity. (c) Normalized integrated intensities of $^{27}$Al signals from the bulk, 1st, 2nd, and 3rd coordination shells around substituted $\mathrm{Ce}^{3+}$ from the saturation-recovery experiment shown in Figure 7(b). The solid lines show the exponential fit to the data (integrated intensity $= M_z^0(1 - e^{-t/T_1})$). The $T_1$ relaxation time decreases with decreasing $^{27}$Al–$\mathrm{Ce}^{3+}$ distance, indicating increasing $^{27}$Al–$\mathrm{Ce}^{3+}$ interaction strength with decreasing distance.

The internuclear distances from the HIPD/11-BM 295 K Rietveld fit along with isotropic chemical shifts calculated from Equation 1 and actual (fitted) isotropic chemical shifts in Table 4 show the direction of the paramagnetic displacement is correctly predicted for the 2nd and further coordination shells around $Ce^{3+}$. The octahedral $^{27}$Al nuclei nearest a substituted $Ce^{3+}$ is predicted to be displaced in both the positive and negative directions from Equation 1, since these $^{27}$Al nuclei are at differening angles from the anisotropic $Ce^{3+}$ unpaired electron spin density. However, this signal is only displaced in the *negative* direction to $-15$ ppm from the bulk signal around 1 ppm. This indicates that the primary source of the displacement is the Fermi "contact" shift, which is consistent with a de-localization of the $Ce^{3+}$ $4f$ spin density with the nearest octahedral $^{27}$Al nuclei. Equation 1 successfully predicts the direction of the displacements of the next two coordination spheres of octahedral $^{27}$Al around a substituted $Ce^{3+}$ ion. This indicates that the Fermi "contact" shift plays a significant role for only the first coordination sphere of octahedral $^{27}$Al around $Ce^{3+}$, and dipolar interactions ("pseudocontact" interactions) dominates the second and further coordination spheres of octahedral Al near $Ce^{3+}$.

Figure 9(a),(b) shows the excellent fits to the single-pulse $^{27}$Al NMR spectra obtained using these predicted displacement directions for $Y_{2.94}Ce_{0.06}Al_5O_{12}$; similar results are obtained for the other single-pulse $^{27}$Al spectra. The population of the $^{27}$Al nuclei corresponding to the $-15$ ppm signal amounts to 4 times the Ce concentration in the sample. This is consistent with the first coordination shell of octahedral Al atoms around Ce, which contains 4 Al atoms equidistant to Ce (see Table 4). Integration of the signals at 1.3 ppm (bulk), 3.2 ppm (2nd and 3rd shells), $-1.2$ ppm (3rd shell), and $-15$ ppm (1st shell) yields populations of 71.5 : 12.1 : 7.9 : 8.5, meaning that the largest displaced signal (corresponding to 12 % of the population at 3.2 ppm) is a mixture of the second and third coordination spheres of $^{27}$Al nuclei around $Ce^{3+}$. This leaves the signal at $-1.2$ ppm to be due to half of the 3rd coordination sphere. These paramagnetically-displaced signals have linewidths ($\Gamma$) which range from being equivalent to the bulk signal to being 20 % larger than the bulk signal. The broadening of the spectra is likely primarily due to the effect of paramagnetic $Ce^{3+}$ on the surrounding nuclei,[75] but may also be due to non-uniform environments of the $^{27}$Al nuclei around $Ce^{3+}$. These small Γs indicate a high degree of order and little distortion of the local environment of $^{27}$Al nuclei near substituted $Ce^{3+}$. This supports the Rietveld analysis showing a high degree of crystalline order of the YAG:Ce materials from small ADPs, and the EXAFS results showing small MSRDs of Al atoms around Ce in YAG.

Quantification of the octahedral portion of the $^{27}$Al spectra on its own offers a convincing argument for a random distribution of Ce ions that have been all reduced to $Ce^{3+}$ in the YAG lattice, but this conclusion is further supported by examining the spin dynamics of YAG:Ce. Nuclei near substituted $Ce^{3+}$ are expected to relax much faster than bulk nuclei due to dipolar interactions between $Ce^{3+}$ and nearby $^{27}$Al nuclei.[69] The signal from the faster-relaxing species can be isolated from that of the bulk by simply using a short recycle delay. However, a more elegant method to probe the spin dynamics of these materials is to use a saturation-recovery experiment, which is shown for $Y_{2.94}Ce_{0.06}Al_5O_{12}$ in Figure 7(b). The paramagnetically-displaced octahedral $^{27}$Al signal near $-15$ ppm saturates in intensity much faster than the other octahedral $^{27}$Al signals around 1 ppm, consistent with the conclusion that the $^{27}$Al nuclei which resonate near $-15$ ppm are proximal to $Ce^{3+}$ in the YAG structure. Integrated areas from fits to each spectra result in build-up curves shown in Figure 9(c), from which $T_1$ relaxation times can be extracted by fitting the curves of integrated intensity as a function of time with an exponential function.[76] The measured relaxation time of the signal at 3.2 ppm is the result of a mixture of 2nd- and 3rd-coordination sphere $^{27}$Al nuclei, which means the relaxation time of the 2nd-coordination sphere $^{27}$Al nuclei is likely much less than the value in Table 4, since the 3rd-coordination sphere $^{27}$Al nuclei contributed heavily to the signal intensity of the 3.2 ppm signal. From Figure 9(c) and Table 4 it can be seen that the $T_1$ relaxation time decreases with increasing distance from $Ce^{3+}$ in the YAG structure. This indicates a weaker interaction between $^{27}$Al and $Ce^{3+}$ as the $^{27}$Al–Ce$^{3+}$ distance increases, and supports the fit to the octahedral part of the $^{27}$Al spectra in Figure 9(a).

The tetrahedral $^{27}$Al signal from $Y_{3-x}Ce_xAl_5O_{12}$ is expected to behave analogously to the octahedral signal, but is not as simple to analyze due to the wide Pake pattern which results from a large quadrupolar moment of around 6 MHz.[64] However, a single peak cannot fit the data well, as demonstrated in Figure 9(a), consistent with paramagnetic displacements of the tetrahedral $^{27}$Al signal from proximal Ce$^{3+}$ ions. The first coordination sphere of tetrahedral $^{27}$Al around a substituted Ce$^{3+}$ is in fact shifted to a higher frequency of around 110 ppm, which was only seen by using a field strength of 23.5 T, as discussed presently. Two tetrahedral peaks describes the data around 70 ppm well, as shown in Figure 9(a), with a population of the smaller peak of around 7%. This only matches the concentration of Ce well if this peak is assumed to come from the entire second shell of tetrahedral $^{27}$Al nuclei around Ce$^{3+}$. From a random distribution of Ce$^{3+}$, the population from the second shell of tetrahedral $^{27}$Al nuclei around Ce$^{3+}$ would be 8%, is good agreement with the fitted amount of 7%.

To further investigate the local structure around Ce$^{3+}$ ion in YAG and confirm the model from the 18.8 T measurements, $^{27}$Al measurements were carried out at a high spinning speed of 60 kHz and high field strength of 23.5 T for extremely high resolution. The spectra of $Y_{2.91}Ce_{0.09}Al_5O_{12}$, shown in Figure 10, reveals details of the local structure near Ce$^{3+}$ not observed in the 18.8 T measurements. The same octahedral $^{27}$Al peak near $-15$ ppm with one Ce$^{3+}$ ion in its first coordination shell is still visible, but two peaks near $-30$ ppm are now visible, which are due to octahedral $^{27}$Al nuclei with two Ce$^{3+}$ ions in their first coordination shell. Since the paramagnetic displacement of the signal from $^{27}$Al sites near Ce$^{3+}$ is additive with the amount of Ce nearby, the assignment of the $-30$ ppm peak is consistent with what was observed in the $x = 0.08$ material at 18.8 T, and with what was found in previous studies of paramagnetic ions in solids.[68,69,71] The two peaks near $-30$ ppm indicate two distinct local environments of octahedral $^{27}$Al nuclei with two Ce$^{3+}$ in their

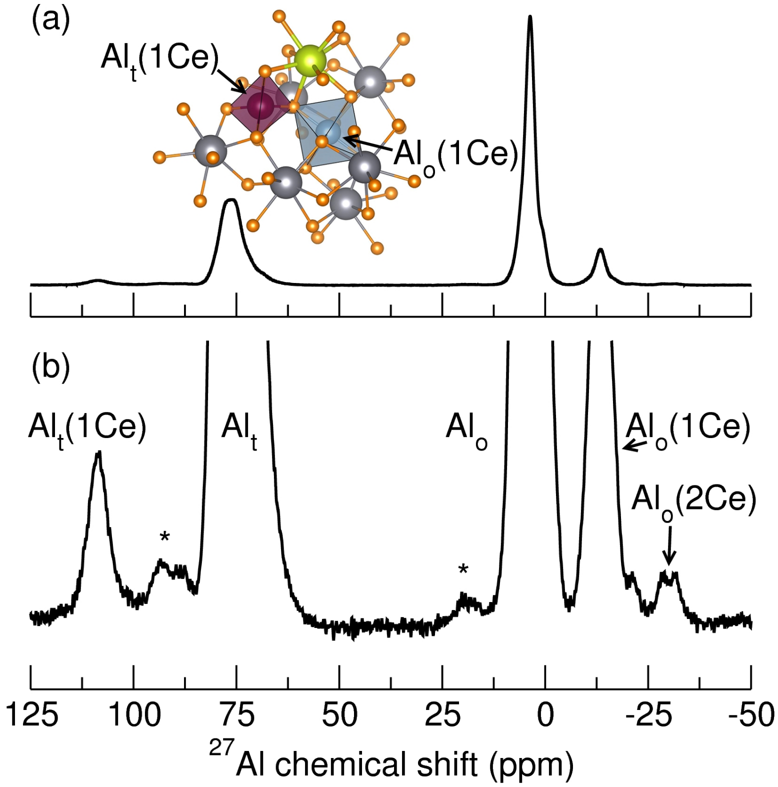

**Figure 10.** (a) Single-pulse solid-state $^{27}$Al MAS NMR spectra of $Y_{2.91}Ce_{0.09}Al_5O_{12}$ acquired at 295 K, 23.5 T, and 60 kHz MAS with (b) a 40× expansion of the intensity axis. Asterisks indicate small amounts of impurities. The inset depicts the local structures of $Al_t$ and $Al_o$ species near one $Ce^{3+}$ dopant ion (depicted by a yellow sphere), which are associated with the signals labeled as $Al_t$(1Ce) and $Al_o$(1Ce).

first coordination shell. There is also a small shoulder on the low-frequency side of the $-15$ ppm peak, which may be due to octahedral $^{27}$Al nuclei with one $Ce^{3+}$ ion in the first coordination shell, and another in a further coordination shell. Measurement of the $T_1$ times confirms the assignment of the peaks, giving relaxation times of 6.5 s for the bulk peak, 138.9 ms for the $-15$ ppm peak (octahedral $^{27}$Al nuclei with one $Ce^{3+}$ in the first coordination shell), and 57.7 ms for the $-30$ ppm peaks (octahedral $^{27}$Al nuclei with two $Ce^{3+}$ in the first coordination shell). The ratio of the bulk peak : $-15$ ppm peak : $-30$ ppm peak from integration of the spectra is 1 : 0.1402 : 0.0073, which compares well with the expected ratio from a random distribution of $Ce^{3+}$, 1 : 0.1237 : 0.0057.

Similarly, the 23.5 T $^{27}$Al spectra sheds new light on the tetrahedral portion of the spectrum, revealing a signal from tetrahedral $^{27}$Al with one $Ce^{3+}$ ion in the first coordination shell, resonating near 110 ppm. The assignment of this peak is again confirmed by relaxation time measurements, which gave a $T_1$ of 1.9 s for the bulk tetrahedral $^{27}$Al peak and 49.9 ms for the 110 ppm peak (due to tetrahedral $^{27}$Al with one $Ce^{3+}$ ion in the first coordination shell). The displacement direction is consistent with the prediction given in Table 4 from Equation 1, and nearly the same value. This suggests the interaction of first coordination shell tetrahedral $^{27}$Al nuclei with $Ce^{3+}$ in YAG:Ce is dominated by the dipolar mechanism, despite the shorter distance between tetrahedral $^{27}$Al and $Ce^{3+}$ compared with octahedral $^{27}$Al nuclei with $Ce^{3+}$. The relative populations of the bulk tetrahedral $^{27}$Al peak : 110 ppm peak from integration are 1 : 0.0503, close to the ratio of 1 : 0.0619 expected from a random distribution of $Ce^{3+}$. The displaced tetrahedral $^{27}$Al peak was not observed in the 18.8 T spectra, possibly due to nearby spinning sidebands or the broad Pake pattern and small population, which likely broadened the signal into the baseline.

A $T_1$-filtered experiment can be used as another confirmation of the previous analysis, since slower-relaxing species, such as the bulk $^{27}$Al signal, can be isolated from faster relaxing species by using a $T_1$-filter. Such an experiment on $Y_{2.94}Ce_{0.06}Al_5O_{12}$ yields the spectra in supporting information Figure S3, which shows an absence of intensity around the $-15$ ppm signal corresponding to the 1st coordination shell of $^{27}$Al around Ce$^{3+}$. There is also missing intensity around the shoulders of the bulk signal, corresponding to the 2nd and 3rd coordination shells of octahedral $^{27}$Al near Ce$^{3+}$. Fits to the octahedral region of the $^{27}$Al NMR $T_1$-filtered spectra and the difference between the single-pulse and $T_1$-filtered spectra confirm the model in Figure 9(b), since in the $T_1$-filtered spectra there is a lack of intensity where the 1st and 2nd shell $^{27}$Al signals would otherwise be in a fully-quantitative 1D single-pulse $^{27}$Al MAS NMR spectra.

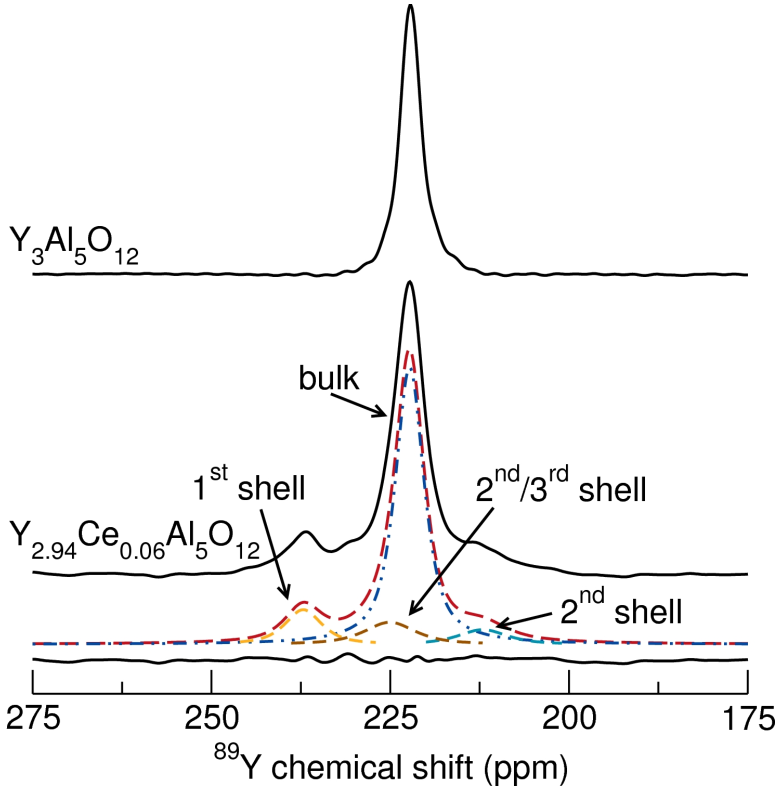

**Figure 11.** 1D single-pulse solid-state $^{89}$Y NMR spectra (6 kHz MAS) of $Y_{3-x}Ce_xAl_5O_{12}$ with (a) $x = 0$ and (b) 0.06 taken at 295 K and 19.6 T. (b) Fit to the $x = 0.06$ Ce$^{3+}$-substituted material, with the difference between the fit and data shown below the spectra. The fit has been offset from the data for clarity.

The paramagnetic effects of the Ce$^{3+}$ ions in $Y_{3-x}Ce_xAl_5O_{12}$ displace the NMR signals of other nuclei as well, such as $^{89}$Y, as shown in the 1D single-pulse solid-state $^{89}$Y MAS NMR spectra in Figure 11. The undoped YAG material shows a single signal at 222 ppm, which agrees well with previous reports.[65,77] Upon Ce$^{3+}$ substitution, a separate signal appears near 237 ppm, the central signal at 222 ppm broadens, and a shoulder appears on both sides of the bulk signal at 222 ppm. These effects are similar to those observed in the $^{27}$Al spectrum, and are due to the paramagnetism of Ce$^{3+}$ in YAG. Equation 1 predicts a $+8$ ppm displacement for two $^{89}$Y nuclei and a $-15$ ppm displacement for the other two $^{89}$Y nuclei in the first coordination sphere ($r = 3.68$ Å) around a substituted Ce$^{3+}$ ion (Table 4). However, it appears the displacement occurs only in the positive direction for the first coordination sphere, indicating the interaction with Ce$^{3+}$ is dominated by the Fermi contact shift, similar to the effects seen in the $^{27}$Al NMR spectra. The displacement direction is in the opposite direction of that observed for the first coordination sphere of octahedral $^{27}$Al nuclei around Ce$^{3+}$ ions. This is consistent with the fact that the Fermi contact shift is inversely proportional to the gyromagnetic ratio of the resonating nucleus, since the signs of these physical constants are opposite for $^{27}$Al and $^{89}$Y nuclei. The next two coordination spheres of $^{89}$Y around a Ce$^{3+}$ ion appear to interact with Ce$^{3+}$ primarily by the through space (dipolar) mechanism. The magnitudes of the calculated displacements are less than the fitted values, which is opposite the trend found in the $^{27}$Al spectra. The integrated population from the $^{89}$Y spectra of $Y_{2.94}Ce_{0.06}Al_5O_{12}$ of the first coordination sphere of Y around Ce$^{3+}$ correspond to $x = 0.0825$, larger than the nominal value of 0.06. However, this is likely due to the very long $T_1$ relaxation time of $^{89}$Y nuclei. Since the $^{89}$Y nuclei near Ce$^{3+}$ will relax faster than other $^{89}$Y nuclei, the $^{89}$Y nuclei near Ce$^{3+}$ ions will have a signal larger than expected if the delay time is not sufficiently long to allow for a fully quantitative spectra, as is likely the case here.

Electron spin density sharing (the Fermi “contact" shift) out to *ca.* 3.6 Å in YAG is consistent with previous observations of interactions of lanthanide-substituted inorganic materials. For example, purely dipolar interactions between paramagnetic lanthanides and $^{19}$F were observed in CaF$_2$ with the next-nearest neighbor at 4.53 Å, but Fermi contact was found to affect the nearest F at 2.63 Å.[78,79] Since the YAG lattice is more covalent than CaF$_2$ (based on O and F electronegativities), Fermi contacts at larger distances are not surprising. Past this first coordination sphere, the pseudocontact shift reasonably predicts the displacement directions and relative magnitudes. The sharing of electron spin density through bonds in YAG reflects the highly connected and compact nature of the structure also observed through the scattering techniques. This connectivity leads to a rigidity that tightly holds $Ce^{3+}$ atoms in YAG:Ce, leading to the large crystal field splitting of $Ce^{3+}$ in YAG and the high quantum efficiency as seen from EXAFS and ADP analyses. The rigidity and reluctance of the YAG lattice to deform, even with such a large dopant ion as $Ce^{3+}$, is also reflected in the very narrow linewidths of the paramagnetically-displaced peaks.

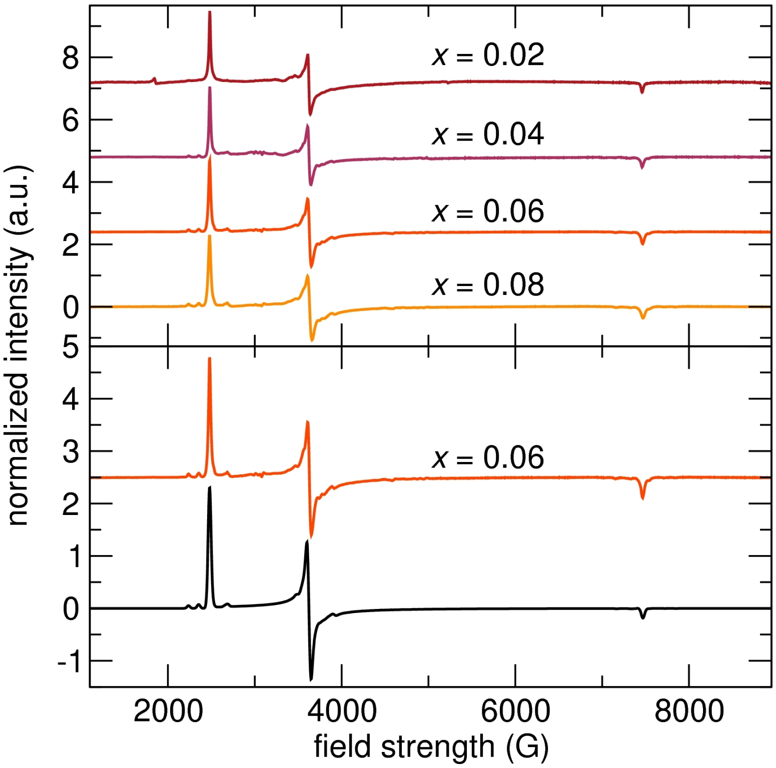

**Figure 12.** Powder EPR data of $Ce^{3+}$ in $Y_{3-x}Ce_xAl_5O_{12}$ taken at 4 K and 9.4 GHz with compositions as labeled in the figure. The bottom spectrum is a simulation of the $x = 0.06$ material with 6 different $Ce^{3+}$ sites.

**Evidence for Ce–Ce pairs by direct observation of the $Ce^{3+}$ electronic environment.** While solid-state NMR spectroscopy is a sensitive tool for probing the local environment of the $^{27}$Al and $^{89}$Y nuclei in $Y_{3-x}Ce_xAl_5O_{12}$, EPR can be used on phosphor materials to inves-

**Table 5. Components of the $g$-tensor from the powder EPR spectra of $Y_{2.94}Ce_{0.06}Al_5O_{12}$ taken at 4 K and 9.4 GHz. The rows of $g$-factor components do not necessarily imply that the each row is from the same Ce site.** [a]

| $g_x$ | $g_y$ | $g_z$ |
|---|---|---|
| 3.03 | 1.94 | 0.946 |
| 2.88 | 1.90 | 0.924 |
| 2.73 | 1.86 | 0.908 |
| 2.69 | 1.81 | 0.899 |
| 2.55 | 1.79 | 0.878 |
| 2.52 | 1.73 | 0.864 |

tigate the local environment of the activator ions' unpaired electrons. The EPR spectra of $Ce^{3+}$ in $Y_{3-x}Ce_xAl_5O_{12}$ ($x = 0.02, 0.04, 0.06, 0.08$) in Figure 12 (taken at 4 K) shows the primary $Ce^{3+}$ signals with $g$-tensor values of 2.73, 1.86, and 0.908 (from left to right). These values are in good agreement with values previously measured and calculated in the literature,[80,81] and the broad range of $g$-tensor values indicates a large electron spin density anisotropy. Spectra from YAG:Ce materials with varying Ce concentrations show the same features. Similarly to the 1D single-pulse solid-state $^{27}$Al MAS NMR spectra, the solid-state EPR spectra of YAG:Ce prepared with and without $BaF_2$ and $NH_4F$ fluxes looks nearly identical, as shown in Figure S2(b). This corroborates the $^{27}$Al NMR result that $BaF_2$ and $NH_4F$ fluxes do not affect the local environment of $Ce^{3+}$ in the YAG lattice. Double integration (DI) of the EPR spectra yields a linear increase in DI value with Ce content (supporting information Figure S4(b)), suggesting all Ce is incorporated into the YAG lattice and is reduced to $Ce^{3+}$ during the reaction, corroborating the XANES, synchrotron X-ray, and $^{27}$Al NMR results. The $\Gamma$ of the main signal in the EPR spectra at $B_o = 2480$ G varies linearly with Ce concentration (supporting information Figure S4(a)), which indicates the presence of Ce–Ce dipolar couplings.[82] Small satellite signals reside near the main $Ce^{3+}$ signals, which have been previously attributed to $Ce^{3+}$ in slightly disturbed (distinct) lattice sites in both

YAG[80] and $YAlO_3$[83] EPR spectra. There appear to be six distinct Ce sites in the YAG:Ce lattice, manifesting six sets of distinct $g$-tensor values shown in Table 5. The small satellite signals are present near all three major features in the spectra, shown in supporting information Figure S5. A simulation using the parameters in Table 5 shown at the bottom of Figure 12 shows that the data can be simulated well with six distinct Ce sites.

To confirm that the satellite signals were from $Ce^{3+}$ and not another unpaired electron, temperature-dependent EPR spectra were taken for the $Y_{2.94}Ce_{0.06}Al_5O_{12}$ material. Since the satellite signals remained present, and broadened at the same rate as the main YAG:Ce signals with increasing temperature, the satellite signals were confirmed to come from $Ce^{3+}$ in YAG. The linewidths of the peaks were found to follow the Orbach law, and the $\gamma$ of the signal at 2480 G was fitted using the equation $\Gamma = (e^{\Delta/k_BT)} - 1)^{-1} + C$.[84,85] From the fit shown in supporting information Figure S4(c), a value of $14\,\mathrm{cm}^{-1}$ was obtained, which is the splitting between the lowest two $^2F_{5/2}$ levels of $Ce^{3+}$.

A previous EPR study attributed the satellite peaks to Ce in disturbed lattice sites, but was unspecific as to what the perturbation was.[80] A separate study correlating the concentration of Ce in YAG to the optical properties suggested that some lower-energy $Ce^{3+}$ sites are present in YAG:Ce, which may be due to perturbed lattice sites or Ce–Ce pairs in the structure.[16] For the $x = 0.06$ material measured here, a random distribution of Ce in the lattice would result in about 8% of Ce–Ce pairs. A fit to the $g_x$ region (shown in supporting information Figure S5) reveals the population of the satellite peaks in the EPR spectrum constitutes around 8.8 % of Ce ions. This agrees quite well with the population of Ce–Ce pairs expected for a random distribution of Ce in the YAG lattice of 8%, suggesting that the satellite peaks and previously observed lower-energy $Ce^{3+}$ sites result from two Ce atoms in neighboring and/or nearby Y sites. This also corroborates the RMC and $^{27}Al$ NMR results, which are consistent with a random distribution of Ce in the YAG lattice. The EPR result also agrees well with the 23.5 T $^{27}Al$ NMR results, which showed that there are at least two distinct environments of octahedral $^{27}Al$ nuclei with two $Ce^{3+}$ ions in their first coordination shell.

## CONCLUSIONS

A combined spectroscopic and scattering study has revealed detailed insights about the local structure of the $Ce^{3+}$ ion in $Y_{3-x}Ce_xAl_5O_{12}$. Synchrotron X-ray scattering showed that the YAG unit cell expands slightly with increasing amounts of Ce (about a 0.03% increase from $x = 0$ to $x = 0.06$). Ce K-edge XANES and $^{27}$Al NMR results show that all the Ce in the YAG lattice is reduced to $Ce^{3+}$, and that the lattice near substituted Ce is well ordered and rigid. Ce K-edge EXAFS reveals a 3% expansion in Ce–O bond distance compared to the Y–O average structure distance, and small MSRDs near Ce, which is related to the high quantum efficiency in YAG:Ce. The distortion of the YAG lattice around substituted Ce decreases with increasing distance from Ce, and is measurable up to the 5th coordination shell (3.7 Å) from the EXAFS data presented here. Analysis of ADPs and calculation of the Debye temperature from the ADPs shows YAG is a very rigid lattice, with many phonon modes being unaccessible at LED operating temperatures. The observed decrease in $\theta_D$ with increasing Ce substitution is related to the quenching of luminescence with increasing Ce substitution, since more phonon modes are available at a given temperature for YAG materials with a higher Ce content. RMC simulations, $^{27}$Al NMR spectra, and EPR results are all consistent with a random distribution of Ce in the YAG lattice. $^{27}$Al and $^{89}$Y NMR experiments also show that the unpaired $4f$ electron in $Ce^{3+}$ causes a displacement in the NMR signal of nearby nuclei, as well as a greatly shortened $T_1$ relaxation time of nearby nuclei. Integration of $^{27}$Al NMR results with Ce composition show the nominal amount of Ce is indeed randomly incorporated into the lattice as $Ce^{3+}$. EPR spectra of the YAG:Ce phosphor show small satellite signals around the main absorption signals, resulting from Ce–Ce pairs present in the amount expected from a random distribution of Ce in the YAG structure.

## Acknowledgement

The authors thank Ryan Davis for advice on EXAFS fitting, Dr. Alexander Mikhailovsky for assistance with the quantum efficiency measurements, and Joan Siewenie for assistance with collection of the neutron powder diffraction data. N.C.G. has been supported by the ConvEne IGERT Program (NSF-DGE 0801627). The research made extensive use of the Central Facilities of the UCSB Materials Research Laboratory, which is supported by the MRSEC Program of the NSF under Award No. DMR 1121053; a member of the NSF-funded Materials Research Facilities Network (www.mrfn.org). We also acknowledge support from the Center for Scientific Computing at UCSB, supported by NSF MRSEC (DMR-1121053) and NSF CNS-0960316. Use of the Advanced Photon Source at Argonne National Laboratory was supported by the U. S. Department of Energy, Office of Science, Office of Basic Energy Sciences, under Contract No. DE-AC02-06CH11357. This work benefited from the use of NPDF and HIPD at the Lujan Center, funded by DOE Office of Basic Energy Sciences; LANL is operated by Los Alamos National Security LLC under DE-AC52-06NA25396. The solid-state NMR measurements at 23.5 T were conducted at the Centre Europeén Champs Haute RMN in Lyon, France. We acknowledge support from the Agence Nationale de la Recherche (ANR 08-BLAN-0035-01 and 10-BLAN-713-01).

## References

(1) Nakamura, S.; Fasol, G.; Pearton, S. J. *The Blue Laser Diode: The Complete Story*, 2nd ed.; Springer, 2000.

(2) Shimizu, Y.; Sakano, K.; Noguchi, Y.; Moriguchi, T. Light emitting device having a nitride compound semiconductor and a phosphor containing a garnet fluorescent material. 1999; U.S. Patent 5,998,925.

(3) Reeh, U.; Höhn, K.; Stath, N.; Waitl, G.; Schlotter, P.; Schneider, J.; Schmidt, R. Light-

radiating semiconductor component with a luminescence conversion element. 2004; U.S. Patent 6,812,500B2.

(4) Doxsee, D. D.; Setlur, A. A.; Brown, Z. R.; Srivastava, A.; Comanzo, H. White light LED device. 2005; U.S. Patent 6,963,857B2.

(5) Shur, M. S.; Zukauskas, R. *P. IEEE* **2005**, *93*, 1691–1703.

(6) Krames, M. R.; Shchekin, O. B.; Mueller-Mach, R.; Mueller, G. O.; Zhou, L.; Harbers, G.; Craford, M. G. *J. Disp. Technol.* **2007**, *3*, 160–175.

(7) Blasse, G.; Bril, A. *Appl. Phys. Lett* **1967**, *11*.

(8) Nakamura, S.; Mukai, T.; Senoh, M. *Appl. Phys. Lett.* **1994**, *64*, 1687–1689.

(9) Yen, W. M.; Shionoya, S.; Yamamoto, H. *Phosphor Handbook*, 2$^{nd}$ ed.; Taylor & Francis Group, 2007.

(10) Blasse, G. *J. Chem. Phys.* **1967**, *47*, 5139.

(11) Ronda, C. R. *Luminescence: From Theory to Applications*; John Wiley & Sons, 2004.

(12) Bachmann, V.; Ronda, C.; Meijerink, A. *Chem. Mater.* **2009**, *21*, 2077–2084.

(13) Robbins, D. J. *J. Electrochem. Soc.* **1979**, *126*, 1550–1555.

(14) Tien, T. Y.; Gibbons, E. F.; DeLosh, R. G.; Zacmanidis, P. J.; Smith, D. E.; Stadler, H. L. *J. Electrochem. Soc.* **1973**, *120*, 278–281.

(15) Robbins, D. J.; Cockayne, B.; Lent, B.; Glasper, J. L. *J. Electrochem. Soc.* **1979**, *126*, 1556–1563.

(16) Setlur, A.; Srivastava, A. *Opt. Mater.* **2007**, *29*, 1647–1652.

(17) Wu, J. L.; Gundiah, G.; Cheetham, A. *Chem. Phys. Lett.* **2007**, *441*, 250–254.

(18) Furman, J.; Gundiah, G.; Page, K.; Pizarro, N.; Cheetham, A. *Chem. Phys. Lett.* **2008**, *465*, 67–72.

(19) Pan, Y.; Wang, W.; Liu, G.; Skanthakumar, S.; Rosenberg, R.; Guo, X.; Li, K. K. *J. Alloys Compd.* **2009**, *488*, 638–642.

(20) Ghigna, P.; Pin, S.; Ronda, C.; Speghini, A.; Piccinelli, F.; Bettinelli, M. *Opt. Mater.* **2011**, *34*, 19–22.

(21) Gracia, J.; Seijo, L.; Barandiarán, Z.; Curulla, D.; Niemansverdriet, H.; van Gennip, W. *J. Lumin.* **2008**, *128*, 1248–1254.

(22) Muñoz-García, A. B.; Seijo, L. *J. Phys. Chem. A* **2011**, *115*, 815–823.

(23) Wang, J.; Toby, B. H.; Lee, P. L.; Ribaud, L.; Antao, S. M.; Kurtz, C.; Ramanathan, M.; Von Dreele, R. B.; Beno, M. A. *Rev. Sci. Instrum.* **2008**, *79*, 085105–085105–7.

(24) Proffen, T.; Billinge, S. J. L.; Egami, T.; Louca, D. *Z. Kristallogr.* **2003**, *218*, 132–143.

(25) Tucker, M. G.; Dove, M. T.; Keen, D. A. *J. Appl. Crystallogr.* **2001**, *34*, 630–638.

(26) Shoemaker, D. P.; Li, J.; Seshadri, R. *J. Am. Chem. Soc.* **2009**, *131*, 11450–11457.

(27) Tucker, M. G.; Keen, D. A.; Evans, J. S. O.; Dove, M. T. *J. Phys.-Condens. Mat.* **2007**, *19*, 335215.

(28) Yü, Q. M. *Mater. Sci. Forum* **2010**, *663-665*, 177–182.

(29) Xu, S.; Sun, L.; Zhang, Y.; Ju, H.; Zhao, S.; Deng, D.; Wang, H.; Wang, B. *J. Rare Earth.* **2009**, *27*, 327–329.

(30) Bérar, J. F.; Garnier, P. *NIST Special Publ.* **1992**, *846*, 212.

(31) Toby, B. H. *J. Appl. Crystallogr.* **2001**, *34*, 210–213.

(32) Momma, K.; Izumi, F. *J. Appl. Crystallogr.* **2011**, *44*, 1272–1276.

(33) Peterson, P. F.; Gutmann, M.; Proffen, T.; Billinge, S. J. L. *J. Appl. Crystallogr.* **2000**, *33*, 1192–1192.

(34) Egami, T.; Billinge, S. J. L. *Underneath the Bragg Peaks: Structural Analysis of Complex Materials*; Elsevier: Kidlington, Oxford, UK, 2003.

(35) Farrow, C. L.; Juhas, P.; Liu, J. W.; Bryndin, D.; BoÅ¿in, E. S.; Bloch, J.; Proffen, T.; Billinge, S. J. L. *J. Phys-Condens. Mat.* **2007**, *19*, 335219.

(36) McGreevy, R. L. *J. Phys.-Condens. Mat.* **2001**, *13*, R877.

(37) Tucker, M. G.; Keen, D. A.; Dove, M. T.; Goodwin, A. L.; Hui, Q. *J. Phys.-Condens. Mat.* **2007**, *19*, 335218.

(38) Heald, S.; Stern, E.; Brewe, D.; Gordon, R.; Crozier, D.; Jiang, D.; Cross, J. *J. Synchrotron Radiat.* **2001**, *8*, 342–344.

(39) Skanthakumar, S.; Soderholm, L. *Phys. Rev. B* **1996**, *53*, 920–926.

(40) Newville, M. *J. Synchrotron Radiat.* **2001**, *8*, 322–324.

(41) Fenzke, D.; Freude, D.; Fröhlich, T.; Haase, J. *Chem. Phys. Lett.* **1984**, *111*, 171–175.

(42) Woessner, D.; Timken, H. *J. Magn. Reson.* **1990**, *90*, 411–419.

(43) Yesinowski, J. P. *J. Magn. Reson.* **2006**, *180*, 147–161.

(44) Massiot, D.; Fayon, F.; Capron, M.; King, I.; Le Calvé, S.; Alonso, B.; Durand, O., Jean; Bujoli, B.; Gan, Z.; Hoatson, G. *Magn. Reson. Chem.* **2002**, *40*, 70–76.

(45) Stoll, S.; Schweiger, A. *J. Magn. Reson.* **2006**, *178*, 42–55.

(46) Robbins, D. J.; Cockayne, B.; Lent, B.; Duckworth, C. N.; Glasper, J. L. *Phys. Rev. B* **1979**, *19*, 1254–1269.

(47) Brese, N. E.; O'Keeffe, M. *Acta Crystallogr. B* **1991**, *47*, 192–197.

(48) Wynne, R.; Daneu, J. L.; Fan, T. Y. *Appl. Optics* **1999**, *38*, 3282–3284.

(49) Mellergård, A.; McGreevy, R. L. *Acta Crystallogr. A* **1999**, *55*, 783–789.

(50) McGreevy, R. L. *Nucl. Intrum. Meth. A* **1995**, *354*, 1 – 16.

(51) Trzesowska, A.; Kruszynski, R.; Bartczak, T. J. *Acta Crystallogr. B* **2004**, *60*, 174–178.

(52) Shannon, R. D. *Acta Crystallogr. A* **1976**, *32*, 751–767.

(53) Özen, G.; Demirata, B. *Spectrochim. Acta A* **2000**, *56*, 1795–1800.

(54) Willis, B. T. M.; Pryor, A. W. *Thermal vibrations in crystallography*; Cambridge University Press, 1975.

(55) Cowley, J. M. *Diffaction Physics*; North-Holland Physics Publishing, 1981.

(56) Diehl, R.; Brandt, G. *Mater. Res. Bull.* **1975**, *10*, 85–90.

(57) Redfern, S. A. T.; Harrison, R. J.; O'Neill, H. S. C.; Wood, D. R. R. *Am. Mineral.* **1999**, *84*, 299 –310.

(58) Vasylechko, L.; Senyshyn, A.; Trots, D.; Niewa, R.; Schnelle, W.; Knapp, M. *J. Solid State Chem.* **2007**, *180*, 1277–1290.

(59) Aggarwal, R. L.; Ripin, D. J.; Ochoa, J. R.; Fan, T. Y. *J. Appl. Phys.* **2005**, *98*, 103514–103514–14.

(60) Pujol, M. C.; Solé, R.; Massons, J.; Gavaldà, J.; Solans, X.; Zaldo, C.; Díaz, F.; Aguiló, M. *J. Appl. Crystallogr.* **2001**, *34*, 1–6.

(61) Sales, B.; Chakoumakos, B.; Mandrus, D.; Sharp, J. *J. Solid State Chem.* **1999**, *146*, 528–532.

(62) Pauling, L. *J. Am. Chem. Soc.* **1929**, *51*, 1010–1026.

(63) Brog, K.; Jones Jr., W.; Verber, C. *Phys. Lett.* **1966**, *20*, 258–260.

(64) Massiot, D.; Bessada, C.; Coutures, J. P.; Taulelle, F. *J. Mag. Res.* **1990**, *90*, 231–242.

(65) Florian, P.; Gervais, M.; Douy, A.; Massiot, D.; Coutures, J.-P. *J. Phys. Chem. B* **2001**, *105*, 379–391.

(66) Lin, Y. S.; Tseng, Y. H.; Liu, R. S.; Chan, J. C. C. *J. Electrochem. Soc.* **2007**, *154*, P16–P19.

(67) Harazono, T.; Yokota, E.; Uchida, H.; Watanabe, T. *B. Chem. Soc. Jpn.* **1998**, *71*, 2797–2805.

(68) Grey, C. P.; Dobson, C. M.; Cheetham, A. K.; Jakeman, R. J. B. *J. Am. Chem. Soc.* **1989**, *111*, 505–511.

(69) Grey, C. P.; Smith, M. E.; Cheetham, A. K.; Dobson, C. M.; Dupree, R. *J. Am. Chem. Soc.* **1990**, *112*, 4670–4675.

(70) Kuklja, M. M. *J. Phys.-Condens. Mat.* **2000**, *12*, 2953–2967.

(71) Bleaney, B. *J. Mag. Res.* **1972**, *8*, 91–100.

(72) Carrington, A.; McLachlan, A. D. *Introduction to Magnetic Resonance*; Harper and Row: New York, 1967.

(73) Morrison, C. A.; Wortman, D. E.; Karayianis, N. *J. Phys. C: Solid State Phys.* **1976**, *9*, L191–L194.

(74) Freeman, A. J.; Watson, R. E. *Phys. Rev.* **1962**, *127*, 2058–2075.

(75) Van Vleck, J. H. *Phys. Rev.* **1948**, *74*, 1168–1183.

(76) Levitt, M. H. *Spin Dynamics: Basics of Nuclear Magnetic Resonance*, 2nd ed.; Wiley, 2008.

(77) Harazono, T.; Watanabe, T. *B. Chem. Soc. Jpn.* **1997**, *70,* 2383–2388.

(78) Bessent, R. G.; Hayes, W. *Proceedings of the Royal Society of London. Series A. Mathematical and Physical Sciences* **1965**, *285*, 430 –444.

(79) Baker, J. M.; Hurrell, J. P. *Proceedings of the Physical Society* **1963**, *82*, 742–756.

(80) Baur, J.; Schlotter, P.; Schneider, J. *Adv. Solid State Phys.* **1998**, *37*, 67âĂŞ78.

(81) Lewis, H. R. *J. Appl. Phys.* **1966**, *37*, 739.

(82) Abragam, A.; Bleaney, B. *Electron paramagnetic resonance of transition ions*; Clarendon P., 1970.

(83) Asatryan, H.; Rosa, J.; Mareš, J. *Solid State Commun.* **1997**, *104*, 5–9.

(84) Orbach, R. *P. Roy. Soc. Lond. A. Mat.* **1961**, *264*, 458 –484.

(85) Yen, W. M.; Scott, W. C.; Scott, P. L. *Phys. Rev.* **1965**, *137*, A1109–A1112.